Discover Applied Sciences

Research

The formation of the granite complex in the Wuhe Mari area of Bayankala Mountain on the northeastern margin of the Tibetan Plateau: constraints from lithogeochemistry and U–Pb zircon dating

Guanghao Tian[1,2] · **Yanbing Zong**[1] · **Yanping Xue**[1,2]

Received: 21 March 2024 / Accepted: 29 April 2024
Published online: 13 May 2024

Abstract
The granite complex in the Wuhe Mari area lies in the tectonic magma belt of the North Bayankala Mountains on the northeastern edge of the Qinghai-Tibet Plateau. It is located in the middle of the first member of the Changmahe Formation of the Early and Middle Triassic Bayankala Mountains Group. This article presents a systematic study of the petrological and geochemical characteristics and chronology of porphyrite granilite, monzogranite, porphyritic monzogranite and diorite in the granite complex in Wuhe Mari area. The genetic relationship between these four rock types as well as the type of source area and tectonic environment are clarified. Zircon LA-ICP-MS-U–Pb dating shows that the porphyritic granodiorite, monzogranite, porphyritic monzogranite and diorite have ages of 221.0 ± 2.7 Ma, 219.8 ± 3.0 Ma, 216.6 ± 4.3 Ma and 213.4 ± 1.6 Ma, respectively. The petrogeochemical characteristics show that the porphyritic granodiorite, monzogranite and porphyritic monzogranite in the granite complex have the characteristics of high Si, Al_2O_3, K, low Na, Ca, Mg, Fe, K, Rb and Th—Content in the strongly incompatible elements of the granite complex have three, the relative loss of Ba, Ta, Nb, Ce, slight enrichment or no anomaly, the loss of Sm, Hf and Zr, the strong loss of Y and Yb and the aluminum saturation index < 1.1. Combined with the geological data all three samples belong to Type I granite formed in the same collision environment. Based on the lithogeochemical characteristics and the results of U–Pb chronology, these three rock formations are believed to have been formed by a series of magmatic melting events and are the result of homologous magma crystallization and differentiation. The diorite forms in an intraplate tectonic setting as a result of the evolution of co-collision granite to intraplate granite.

Keywords Cause · U–Pb zircon dating · Geochemical features · Wuhe Mari granite · Bayankala area

1 Introduction

The study area is located in the Bayankala Mountain Basin in the hinterland of the Qinghai-Tibet Plateau. The distribution occurs in the Hoh Xili-Songpan-Ganzi area in a northwest-west direction. The area is bounded to the north by the Whale Lake-Animaqing suture belt and borders the North China Plate. It also borders the North Qiangtang-Qamdo landmass to the west of the Jinwulan-Jinshajiang river junction belt to the south. The Qilian metallogenic belt is one of the 20 most important metallogenic belts in China and is known for its rich mineral resources, including gold, copper, tungsten and more. Magmatic activity in the region is limited, ranging from the late Huali west to the late Indosinian.

✉ Guanghao Tian, 358091417@qq.com; Yanbing Zong, zongyb@ustb.edu.cn | [1]School of Civil and Resources Engineering, University of Science and Technology Beijing, Beijing 100083, China. [2]Langfang Center for General Survey of Natural Resources, CGS, Langfang 065000, China.

The Bayankala Basin formed mainly in the Mesozoic as a result of the development of the Tethys Ocean [1]. Recent studies focused on sediment sources, tectonic basin types and bedrock properties and provided significant results: (1) The basin is a Late Permian–Triassic rift-type turbidite basin on the southern edge of the complex structure of the Laoya continent. It is similar to the present-day turbidite basin in the Bay of Bengal [2]. (2) The crust of the Longmuco-Shuanghu-Lancang River is subducted northward, resulting in back-arc basin formation [3]. (3) The Anima Qing is connected to the Mianluo suture zone and is considered a small ocean basin. The main sea basin is in the Sanjiang area. This connection persisted until the Middle Triassic [4, 5]. (4) The Pan described pools is a bidirectional marginal foreland basin [6]. (5) The area is considered a turbidity fan, similar to Benlaga Bay in the Ganges. It serves as a "trash heap" for the denudation products of the Post-Kunlun Orogeny, which are transported and deposited again [7, 8]. (6) Belongs to the Triassic Inland Sea Basin [9–11]. (7) This is a paleorift basin that has a strong depression from the inside out, rather than an oceanic basin, although residual oceanic features are still present [12]. (8) This is a paleorift basin, which has a strong depression from the inside out, rather than an oceanic basin, although it still has residual oceanic features. The basin is a large, contractile, composite rock basin associated with the typical oceanic subduction zone on the north and south sides, namely the Animaqing suture zone and the Hoh-Xili -Jinsha River Seam Belt [13]. The basin has undergone a complex, long-term evolutionary process since the Devonian rifting period. Describe the geologic history of the area, including the expansion of the Carboniferous Ocean, followed by contraction and contraction during the Early to Middle Permian Period. A residual ocean formed in the Late Permian-Middle Triassic period, which eventually became a marine margin foreland basin in the Late Triassic. Previous studies of the volcanic rocks in the Bayankala Basin lacked detailed investigations and chronological evidence. The rock mass on the eastern side was the focus of the investigation and an age value of 185 ± 9 Ma was reliably determined using the potassium-argon method, a method indicating an early Jurassic age in the Indo-Sinian period. Although the biotite mineral was more susceptible to weathering and alteration, resulting in a lower age (new) value, this does not affect the overall confidence in the results. This article reliably compares the genetic relationship between granodiorite and monzogranite of the granite complex in the source area and tectonic environment through petrogeochemical research and zircon U–Pb isotope chronology analysis. The aim of this study is to confidently determine the spatiotemporal coordinates, genetic type, source area nature and tectonic background of the granite complex in the Wuhe Mari area in the North Bayan Kala Mountain tectonic magma belt. The results will significantly contribute to our understanding of the formation and development process of the granite complex in the Wuhe Mari area. This study will improve the understanding of granite formation in the area and provide valuable evidence for future geological exploration and prospecting breakthroughs.

In summary, the author effectively uses the results of the 1:50,000 Lower Warehouse Boundary (I47E010014) and Side Budi (I47E011014) Regional Geological and Mineral Survey in the North Bayankala Mountain Area of Qinghai Province (Project No.: 12120114009001). The paper was carefully compiled after conducting extensive geological field investigations, laboratory experiments, data collection, data processing and theoretical analysis.

2 Regional geological setting

The study area is certainly located in the Bayankala Basin, which is located in the northeast of the Qinghai-Tibet Plateau. It is bounded by the Muzitag-Kunlun-Animaqing suture belt in the north, the East-Kunlun-West-Qinling orogenic belt, the West-Jinwulan-Yushu-Jinshajiang and Qiangtang-Qamdu suture belt in the south, and the Longmenshan tectonic belt and the Yangtze River landmass in the south Southeast. The Qinghai-Tibet Plateau consists of the East Kunlun Formation (EKL), Bayankala Formation (BY), Qiangtang Formation (OT), Lhasa Formation (LS) and Gangdis Formation (GDS). The article confidently discusses various suture belts and introduces the Muzitag-Kun-Animaqing suture belt (KLANS), the Xijin-Ulan-Yushu-Jinsha River suture belt (XJ-JSJS), the Longmcuo-Shuanghu suture belt (LSS), and the Pangong Lake-Nujiang suture belt (BG-NJS) and the Ganzi-Tangtang suture belt (GZ-LTS). Furthermore, the importance of the Bayankala Basin is highlighted, as shown in Fig. 1 [14].

The Bayankala Basin was formed by the continuous expansion, collage and collisional orogeny of the New Tethys Ocean since 250 Ma [15, 16], which is part of the massive Indochinese orogeny on the Tibetan Plateau.

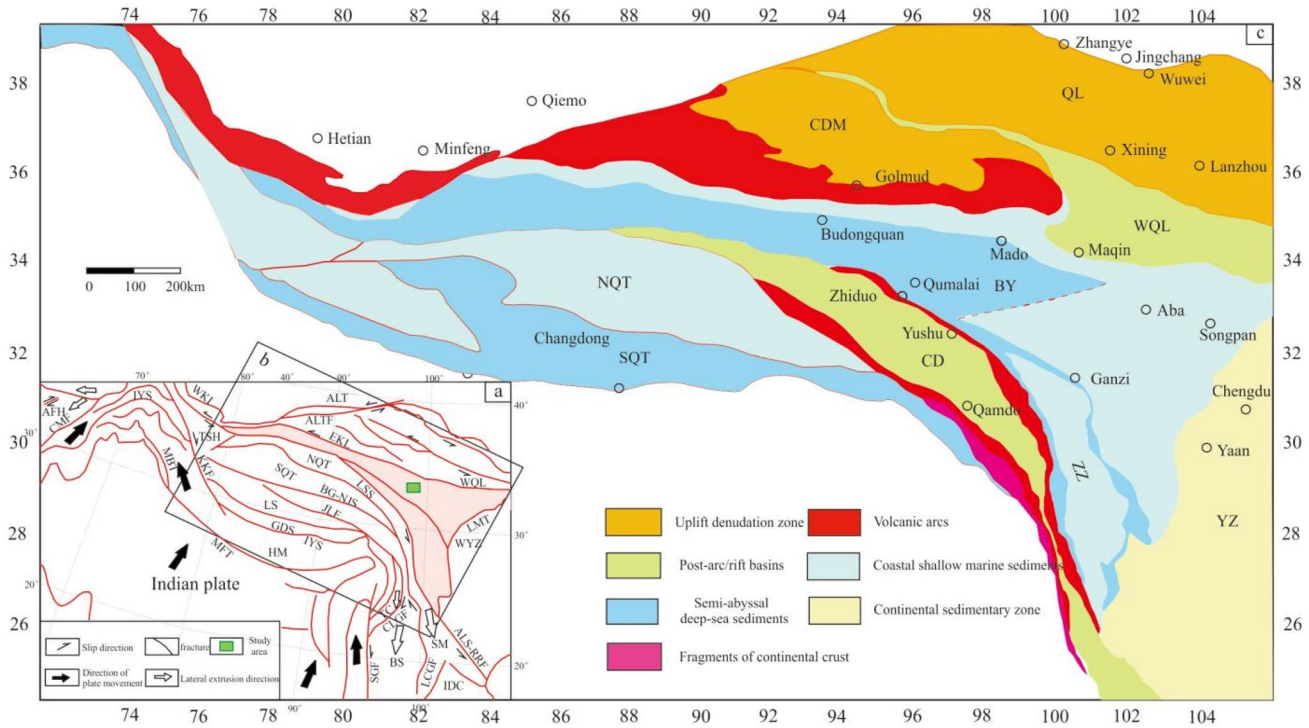

Fig. 1 Geotectonic location map of the study area [15, 17]. AFH. Afghan terrain; ALT.Altyn Grounds; WKL. West Kunlun Formation; QL. Qilian Earth; EKL. East Kunlun Grounds; BY. Bayankala Terti; NQT. North Qiangtang landmass; SQT. South Qiangtang Ground; YZ. Yangtze landmass; ZYA. Zhiduo-Yushu-Jiangda volcanic arc; LS. Lhasa Tertiform; TC. Tengchong Earth; BS.Baoshan landmass; SM. Simao Ground; HM. Himalayan lands; GDS. Gangdis Terres; CD. Qamdo Body; ZZ. Zhongzan Ground; KL-ANS. Muzitag-Kunlun-Anima Qing suture belt; XI-JSJS. Xijin Ulan-Yushu-Animaqing suture belt: LSS.Longmucuo Shuanghu suture zone; BG-NJS. Bangong Lake Nujiang suture zone; IYS. India the Yarlung Zangbo River suture zone; ALTF. Altyn tagh fault; GZ-LTS. Ganzi Litang suture zone; ALS-RRF. Ailaoshan Honghe Fault; GLGF. Gaoligong Fault; JLF. Jiali Fault; LMT. Longmen Mountain tectonic belt; SGF, Sagaing fault; MBT. Boundary thrust fracture; MFT. Main forward thrust fault; KKF. Karakoram Fault; CME. Chaman Fault

3 Petrological features

The Wuhe Mari granite complex is mainly composed of granodiorite and monzogranite lithologies. Monzogranite and granodiorite have different origins, with monzogranite forming from rock foundations and granodiorite occurring in small rock masses. The Wuhe Mari area exposes monzogranite covering an intrusive area of about 23.4 km^2. The monzogranite is in intrusive contact on the north and east sides with the first member of the Early and Middle Triassic Changmahe Formation of the Bayankala Mountain Group. The contact surface has a steep outward inclination angle of 45°-65° and a curved shape. The surrounding rock exhibits significant angular changes, and outside the rock mass is a trap body of surrounding rock. The intrusion extends into the surrounding rock. To the west (Fig. 2) it pulses against medium-fine-grained monzogranite ($\pi\gamma\delta T_3$) and to the south it borders preserved porphyry medium-fine-grained monzogranite ($\pi\gamma\delta T_3^1$). The outcrop is of good quality and has well-developed rock joints. However, some sections are unsuitable for the formation of embankment gravel.

The rock is definitely medium-coarse granodiorite with a striking similarity to porphyry ($\pi\gamma\delta T_3^2$). The outcrop area measures approximately 1.1 km^2. Two exposed intrusions can be seen in the northern part of the study area. One of these intrusions has the shape of a long strip, while the other is a small rock bead with a planar shape. The rock formation is in contact with porphyry medium-fine-grained granodiorite ($\pi\gamma\delta T_3^1$) and medium-fine-grained diorite (δT_3). The diorite was penetrated and cut by a canyon, now covered by Quaternary alluvium.

The sample provided is a medium-fine-grained monzogranite (ηγT3) with a weathered surface that appears gray-brown and a fresh surface that appears light gray-white to light gray-red (Fig. 3A). The rock has a medium-fine-grained granite with a block structure. The sample mainly contains plagioclase, potassium feldspar, and quartz minerals, as shown in Fig. 4A. The size of the minerals ranges from 1-2 mm, 0.5-1 mm (fine) and 2-3 mm (medium). The rock contains plagioclase-feldspar grading 25–35%, fine-grained and semi-automorphic to automorphic lamellae, including polyflaky

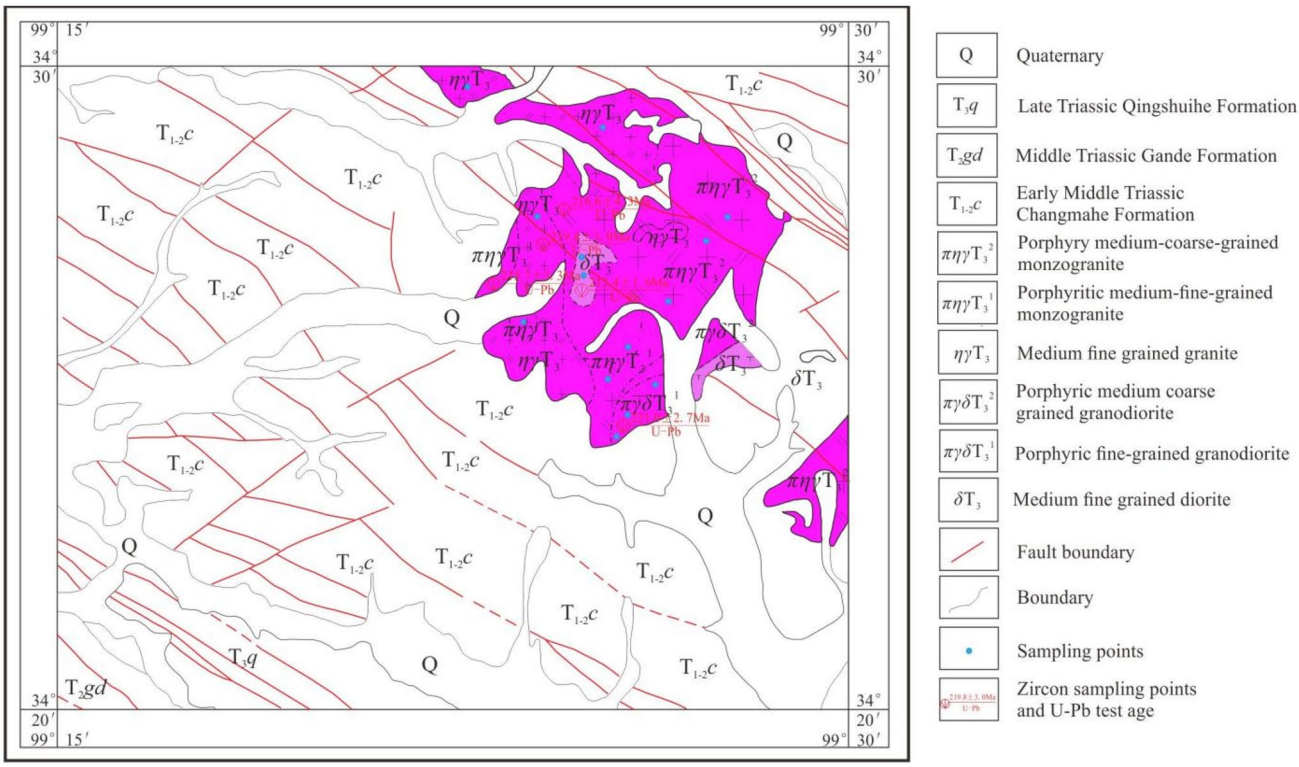

Fig. 2 Schematic geological map of the study area

Fig. 3 Field characteristics of magmatic rock mass. A-Medium-fine-grained monzogranite rock mass fragmented spherical weathering appearance; B-Porphyritic medium-coarse-grained monzogranite rock mass joints and weathered appearance; C-Medium-fine-grained granodiorite; D-Porphyritic medium-fine-grained granodiorite

bicrystals. Potassium feldspar content is 35–40% and appears as semi-automorphic plates, striped bicrystals, fine dendritic striped bicrystals, Karl Paris bicrystals and more. The sample contains 30–35% quartz with fine grains, grains and mostly single-crystal quartz. The crystal plane is relatively clean with a positive edge. Under the orthogonal polarizer, wave-like

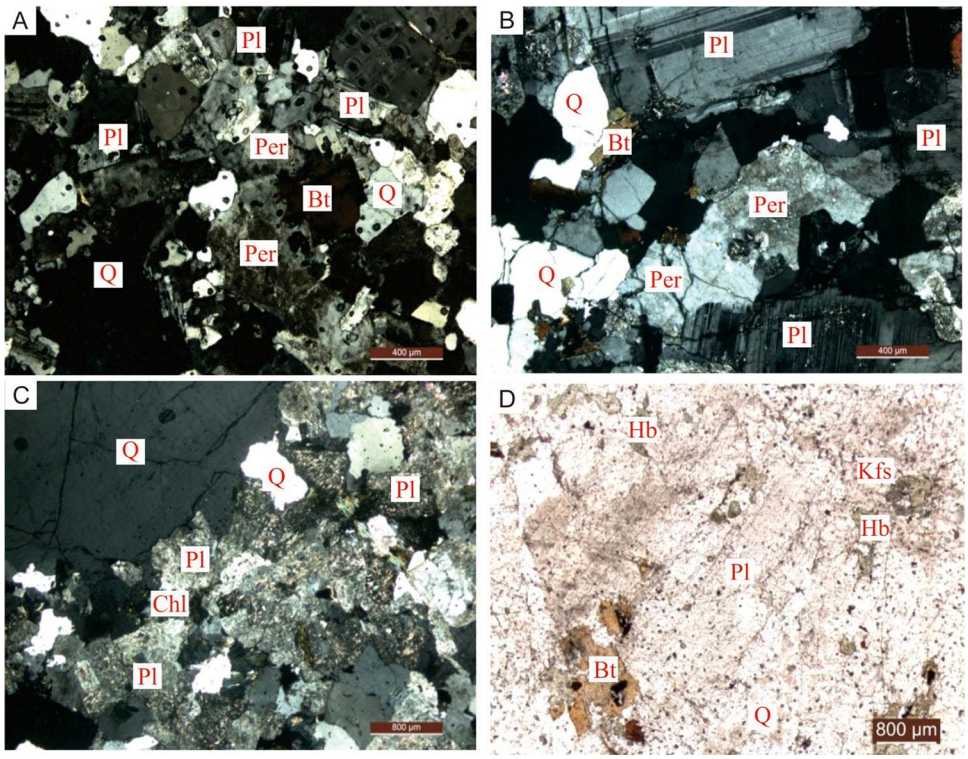

Fig. 4 Microscopic features. A-Medium-fine-grained monzogranite thin sections 10 × 5(+); B-Porphyritic medium-coarse-grained granodiorite thin sections 10 × 5(+); C-Porphyritic medium-fine-grained granodiorite medium thin section identification mineral photo 10 × 5(+); D-diorite thin section identification mineral photo 10 × 2.5 (−); Q. Quartz; Pl. plagioclase; Per-striped feldspar;Bt.biotite

extinction and gray and white interference color are visible. The sample has an alternative culture structure of quartz and feldspar. Biotite is a mineral with a 5% content and a flaky texture. It shows marked pleochroism with a yellow–brown or light brownish-yellow appearance and has a group of complete cleavage. When observed under an orthogonal polarizer, it exhibits parallel extinction and a strong interference color that is often obscured by its own color. The secondary minerals make up 5% of the grade and consist of epidote, apatite and zircon. The epidote content is 2%, and it appears columnar and granular. The apatite content is 2% and appears hexagonal, columnar, needle-like and granular. The zircon content is negligible and appears columnar with bipyramid at both ends generally.

The rock is identified as porphyritic medium-coarse-grained monzogranite ($\pi\eta\gamma T_3$). The weathered surface appears gray-brown, while the fresh surface is gray-white and gray-red. The porphyry structure is clear with a coarse-grained granite structure in the matrix and a massive structure. The rock consists of two different parts: porphyry and matrix. The porphyry content, which is mostly coarse and irregularly grained, consists of plagioclase and a small amount of potassium feldspar accounting for 5–8% of the rock (Fig. 3B). The outcrop in the field contains both short and long columnar crystals as well as a small amount of rounded crystals. These crystals are randomly arranged and unevenly distributed, giving the appearance of scattered stars. The matrix content is between 92 and 95% and shows a medium-coarse-grained granite structure (Fig. 4B). Rocks are made up of primary, secondary, and accessory minerals. The main minerals in the sample contain plagioclase, potassium feldspar and quartz. The plagioclase content is between 25 and 35% and is semi-automorphic and platy with a disordered distribution. The mineral size is between 6 and 2 mm. The potassium feldspar content is between 45 and 35%, with a disordered distribution, while the granular and italic quartz content is between 21 and 25%. Biotite is the secondary mineral present with a low content of approximately 4%. It has undergone metasomatization by chlorite and muscovite minerals, mostly in flake form. The secondary minerals consist of apatite and zircon, where apatite is columnar, acicular and granular and zircon is columnar. Both minerals have a low content. The rocks undergo a weak alteration process that results in the formation of minerals such as sericite, kaolin, chlorite and muscovite.

The rock is identified as a porphyritic medium-coarse granodiorite ($\pi\gamma\delta T_3$). The weathered surface shows a gray-brown color, while the fresh surface shows a gray-white or light gray-white hue. It has a porphyry structure with medium-coarse-grained granite in the matrix and a massive structure. The rock consists mainly of two components: porphyry and matrix. The porphyritic crystals, which make up 10–15% of the rock, consist of plagioclase and a small amount of potassium feldspar. Porphyritic grains range in size from 2–4 mm to 4.5–5 mm, with most being coarse and irregular granular grains. The crystal shape on the outcrop in the field is relatively regular, with short and long columnar crystals visible and some

slight opacities. The matrix consists of major, minor and secondary minerals accounting for 85–90% of the content. The minerals have a maximum crystal size of 1 × 3 cm, with coarse minerals generally between 5 and 7 mm and fine minerals between 1 and 2 mm. The mineral content of the sample consists mainly of plagioclase feldspar, potassium feldspar and quartz. Plagioclase feldspar is the most abundant mineral, accounting for 45–30% of the sample. The crystals are semi-automorphic, columnar, granular crystals and often have a ring structure with a slight sericite in the center of the ring. Potassium feldspar typically contains 20–25% of the mineral, with microcline being the predominant form and having a granular form. Notably, a worm-like structure is often observed on the side of the potassium feldspar that comes into contact with plagioclase. The quartz content is between 25 and 30% and is distributed in the intergranular space of other minerals in the form of grains. Secondary mineral content is 5% and consists primarily of biotite in flake crystals, with some showing slight chlorite phenomena along the cleavage fracture. The secondary mineral content is 2% and consists of epidote, apatite and zircon. Epidote is granular, columnar, light yellow -green and unevenly distributed. Apatite is granular, needle-shaped and hexagonal. Zircon is columnar and often bipyramidal at both ends. Porphyry crystals are unevenly distributed in rocks and have different concentrations. The bedrock projection of the rock mass is generally visible and spherical weathering patterns are observed in good sections. In contrast, stones in poor sections are broken, producing gravel of varying sizes, which is distributed along the slope and ditch.

The rock described is a porphyritic medium-fine-grained granodiorite ($\pi\gamma\delta T_3$). The weathered surface appears gray-brown, while the fresh surface is gray-white or light gray-white. The rock has a porphyry structure with fine-grained granite structure in the matrix and a massive structure (Fig. 3C). The rock consists of two different parts: porphyry and matrix. The porphyritic crystal content consists of 10–15% plagioclase and a small amount of potassium feldspar. Porphyry grain size ranges from 3–4 mm to 4–5 mm, with most being coarse, irregularly grained crystals that have a scattered star distribution. The spotted crystals (Fig. 4C) on the outcrop in the field have an irregular crystal shape, consisting of short columnar crystals, long columnar crystals, and some round crystals. The crystal size is limited to a maximum of 0.5 × 2 cm. The matrix content consists of 85–90% major minerals, minor minerals and secondary minerals with a size range of 4–0.5 mm (medium), less than 1–2 mm and less than 0.5–1 mm (fine). The main mineral content is 81–87% and consists of plagioclase, quartz and a small amount of potassium feldspar. The plagioclase content is 40–50%, is semi-automorphic, plate-shapedwith a disordered distribution. The quartz content is 35–30%, with semi-automorphic granular. The potassium feldspar content is 7–6% and exhibits semi-automorphic, granular, scattered and void-filling properties. Secondary minerals make up 3–4%, including flake-shaped biotite with significant pleochroism in yellow–brown to light brownish-yellow. Complete fission is visible and parallel extinction and high interference color can be observed under orthogonal polarizer, although this is often masked by its own color. In addition, secondary altered chlorite can be found at the edges. Biotite fades over time. The secondary minerals present are epidote, apatite and zircon. Epidote is columnar, granular, and light yellow-green in color. Apatite is hexagonal and needle-shaped, while zircon is columnar and often bipyramidal at both ends. Porphyritic crystals are distributed unevenly in the rock.

The rock described is a medium-fine-grained granodiorite ($\gamma\delta T_3$). Its weathered surface appears gray–brown, while the fresh surface is gray–white–light gray. The rock has both a medium-fine-grained granite structure and a massive structure. Rocks consist of major, minor and secondary minerals and vary in size from fine (1–2 mm), very fine (less than 0.5–1 mm) and medium (2–5 mm), to coarse (larger than 6.5 mm). The major minerals are 97–95% plagioclase, potassium feldspar and quartz, and plagioclase is 57–60% plagioclase, semi-automorphic and disordered (Fig. 4D).The rock was metasomatized by sericite, with a potassium feldspar content of 10–15%. The feldspar is granular, scattered and gap-filling with micro-oblique stripes. The quartz content is 20–30% and is semi-automorphic with a granular and disordered distribution, with a small proportion of gap-filled distribution. The surface is fresh and clean. The low mineral content consists of 3–5% biotite flakes. In addition, epidote, apatite and zircon are present as secondary minerals. Epidote is unevenly distributed and appears columnar, granular, and light yellow-green. Apatite is granular, hexagonal and needle-shaped, while zircon has a columnar shape.

4 Analysis methods

4.1 Whole rock chemical composition

The geochemical samples consist of medium-fine-grained monzogranite, porphyritic medium-fine-grained monzogranite, porphyritic medium-coarse-grained monzogranite, porphyritic medium-fine-grained granodiorite and granodiorite.

The testing and analysis of major, trace and rare earth rock elements were completed at the Wuhan Mineral Resources Supervision and Testing Center and the Experimental Testing Center of the Xi'an Institute of Geology and Mineral Resources. The Panalytical Axios XRF and Thermo X-Series II ICP-MS demonstrated better accuracy than 1% and 5%, respectively.

Fourteen geochemical samples were tested. The samples included 3 pieces of medium-fine-grained monzogranite, 3 pieces of porphyritic medium-fine-grained monzogranite, 3 pieces of porphyritic medium-coarse-grained monzogranite, 3 pieces of porphyritic medium-fine-grained granodiorite and 2 pieces of granodiorite. The analysis results are shown in Table 1.

4.2 Zircon U–Pb dating

This work systematically investigates the zircon U–Pb chronology of an igneous rock mass. Five samples, including a piece of medium-fine-grained monzogranite (PM006-4-TW1), were collected from various rocks within the rock body. The sample consists of four rock pieces: two of porphyritic medium-fine-grained monzogranite (PM006-1-TW1, PM006-7-TW1), and one of porphyritic medium-fine-grained granodiorite (PM005-1-TW1) and one of medium-fine-grained diorite (D1685-TW1). The Experimental Test Center of Xi'an Institute of Geology and Mineral Resources carried out zircon U–Pb isotope dating using laser plasma mass spectrometry laboratory (LA-ICP-MASS).

The analysis and testing of zirconium U–Pb isotope dating was carried out using the Neptune multi-receiver plasma mass spectrometer manufactured by the German company Finnigan and equipped with the UP213nm laser ablation system of the American New Wave company. The experimental data were preprocessed using the ICP-MS Data Cal 4.3 program. The harmonic diagram of the zircon age and the frequency histogram were created using the program Isoplot 3.0. Hou Kejun describe the experimental testing process clearly and concisely [18].

5 Analysis results

5.1 Geochemical characteristics of whole rocks

The Wuhe Marihe granite complex consists of five acidic rock units with a SiO_2 content of 67.9% to 77.30%, an Al_2O_3 content of 12.13% to 15.16% and a total alkali content ($K_2O + N_2O$) of 3.11% to 8.35%. The K_2O/Na_2O ratio is between 0.32% and 1.43%. In addition, the MgO and TiO_2 contents are between 0.06% to 1.4% and 0.07% to 0.5%, respectively. The CIPW standard mineral grade indicates a quartz content between 24.54% and 38.59%. In addition, the SiO_2 content of the rock is supersaturated. The A/CNK index is between 1.018 and 1.253. The DI ranges from 77.46 to 95.37, while the SI ranges from 0.65 to 15.96. Based on the Q-P-A and TAS plots (Fig. 5), the sample falls within the granite-granodiorite-alkaline gabbro range. In the SiO_2-AR diagram (Fig. 6A), the sample lies in the alkaline-granodiorite-alkaline range. The A/CNK-A/NK plot (Fig. 6B) shows the sample falls in the peraluminous-quasiluminous region.

The monzogranite is medium-fine grained and has a SiO_2 content in the range of 75.53% to 77.30%, confirming its acidic characteristics. Al_2O_3 content 12.23%—12.31%; TiO_2 content 0.06%—0.11%. The K_2O content is 4.43%—4.88%, the Na_2O content is 3.13%—3.49% and $K_2O > Na_2O$, and the rock contain a lot of Si, Al and K, little Na content and poor content in Ca, Mg and Fe. The rock is identified as calcium-alkaline based on the Ritman index of $\delta = 1.89–1.98$, $\delta < 4$. It has a high alkalinity index of AR = 4.17–4.645 and a low consolidation index of SI = 0.656–1.548. The degree of magma differentiation is high, resulting in highly acidic rock. The differentiation index of DI = 92.44–95.37 and the felsic index of FL = 91 both confirm the high acidity of the magma. The felsic composition of the rock is characterized by a high content of SiO_2 and K_2O and a low content of FeO, MgO and CaO. The values of 939–94.70 for the Silica Saturation Index (SSI) and 91.176–94.595 for the Mafic Index (MF) reflect a high degree of magma separation and crystallization. The high acidity of the rock is indicated by the Larsen index (LI) of 26.127–29.242. Table 2 clearly shows the CIPW standard minerals, with the rock notably lacking the standard mineral diopside, but containing the standard mineral corundum. The standard mineral combination of Q, Or, Ab, An, C, Hy clearly shows that the rock belongs to the supersaturated type SiO_2 with supersaturated aluminum.

The porphyry medium-grain monzogranite is an acidic rock with a SiO_2 content in the range of 71.30% to 74.60%. The sample contains 13.42% to 14.38% Al_2O_3, 0.15% to 0.32% TiO_2, with a higher K_2O content of 4.11% to 4.83% and a Na_2O content of 3.51% to 3.70%. The rock is safely classified as calc-alkaline with an index of $\delta = 2.08–2.19$ and $\delta < 4$. Its alkalinity index is AR = 2.953–3.656 and its consolidation index is SI = 2.582–5.877. The degree of magma differentiation

Table 1 Analysis results of the chemical composition of the magmatic rock mass in the working area

Sample	PM006-4-YH1*	PM006-5-YH1*	PM006-5-YH2*	PM006-6-YH1*	PM006-6-YH2*	PM006-7-YH2*	PM005-12-YH3	PM005-12-YH4	D1683-YH1	PM005-3-YH2	PM005-3-YH3	PM005-3-YH4	D1685-YH1	D1685-YH2*
Name	MFGM	MFGM	MFGM	PMFGM	PMFGM	PMFGM	PMCGM	PMCGM	PMCGM	PMGG	PMGG	PMGG	GD	GD
SiO_2	76.4	76.5	76.7	71.3	74.6	71.7	71.8	72.1	71.47	68.6	68.6	68.7	50.42	50.9
TiO_2	0.08	0.11	0.07	0.32	0.15	0.32	0.42	0.41	0.28	0.59	0.61	0.59	2.07	2.09
Al_2O_3	12.23	12.31	12.43	14.38	13.42	14.3	14.11	13.9	13.77	14.95	15.12	14.6	15.99	16.05
Fe_2O_3	0.23	0.05	0.03	0.24	0.11	0.29	0.52	0.63	2.79	0.69	0.55	0.57	10.43	0.51
FeO	1.4	1.5	1.1	2.4	1.4	2.2	2	1.9	1.4	2.2	2.3	2.3	0.5	9
MnO	0.03	0.04	0.04	0.04	0.03	0.04	0.05	0.05	0.043	0.06	0.05	0.05	0.15	0.15
MgO	0.11	0.15	0.07	0.63	0.26	0.64	0.69	0.66	0.53	1.22	1.24	1.4	6.81	6.89
CaO	0.7	0.7	0.7	1.6	1.2	1.3	1.9	1.7	1.69	2.8	2.8	2.4	9.29	9.6
Na_2O	3.13	3.4	3.36	3.7	3.51	3.63	3.16	3.15	3.59	3.16	3.21	3.14	2.34	2.38
K_2O	4.82	4.59	4.82	4.18	4.83	4.11	4.25	4.37	4.04	4.07	3.98	4.33	0.77	0.78
P_2O_5	0.02	0.02	0.02	0.07	0.04	0.08	0.1	0.11	0.063	0.15	0.15	0.15	0.3	0.3
$H2O^+$	0.5	0.26	0.36	0.5	0.06	0.72	0.8	0.7	0.5	2.13	1.81	2.26	0.4	0.24
Lol	0.95	0.59	0.7	1.17	0.4	1.32	0.72	0.58	0.5	0.2	0.2	0.3	0.5	1.25
La	16.2	17	12.5	24.6	21.8	31.2	62.94	47.8	47.86	52.53	51.15	53.77	16.13	16.4
Ce	38.6	37.6	30.2	52.2	46	60.5	117.2	93.4	86.89	95.34	93.05	98.6	64.02	39.7
Pr	4.51	4.42	3.66	5.41	5.06	7.13	13.85	10.4	5.78	11.05	10.91	11.61	4.57	5.12
Nd	17.4	17	13.9	18.8	18.8	23.5	47.32	35.8	20.56	37.44	37.56	39.57	19.14	21.2
Sm	4.46	4.87	3.44	3.81	4.15	4.93	8.26	6.62	4.33	6.4	6.62	6.68	4.56	5.66
Eu	0.12	0.17	0.1	0.76	0.61	0.84	0.84	0.79	0.75	1.04	1.1	1.09	1.22	1.69
Gd	4.41	5.12	3.57	3.58	3.9	4.28	6.64	5.41	4.44	4.91	5.21	5.34	3.92	5.41
Tb	0.75	0.9	0.58	0.57	0.65	0.68	1.12	0.97	0.74	0.79	0.84	0.84	0.67	0.84
Dy	4.82	5.75	3.54	3.41	3.89	3.61	5.99	5.43	4.2	4.12	4.37	4.35	4.01	4.82
Ho	0.99	1.24	0.76	0.72	0.85	0.75	1.18	1.08	0.83	0.78	0.82	0.82	0.76	0.95
Er	3.01	3.66	2.27	2.1	2.36	2.1	3.33	3.13	3.34	2.13	2.24	2.21	2.42	2.61
Tm	0.48	0.58	0.36	0.34	0.4	0.34	0.54	0.52	0.43	0.33	0.34	0.34	0.28	0.39
Yb	3.26	4.12	2.58	2.19	2.61	2.31	3.52	3.3	2.89	2.08	2.17	2.15	1.77	2.5
Lu	0.48	0.57	0.36	0.34	0.39	0.33	0.45	0.44	0.48	0.28	0.28	0.27	0.29	0.36
Y	28	34.5	21.5	19.4	21.7	19.3	32.13	29.87	28.06	21.43	22.41	22.18	20.49	23.9

MFGM-Medium-fine-grained monzogranite; PMFGM-Porphyritic medium-fine-grained monzogranite; PMCGM-Porphyry medium-coarse-grained monzogranite; PMGG-Porphyritic medium-grained granodiorite; GD-Granodiorite

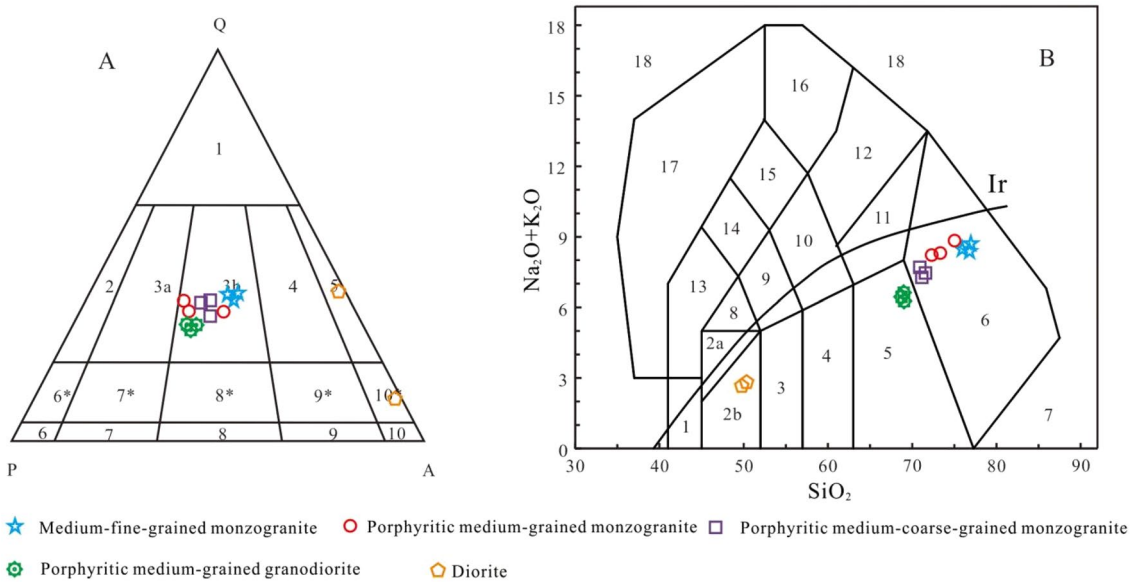

Fig. 5 Q-P-A diagram of magmatic rock mass (**A**) and TAS diagram (**B**) [19, 20]

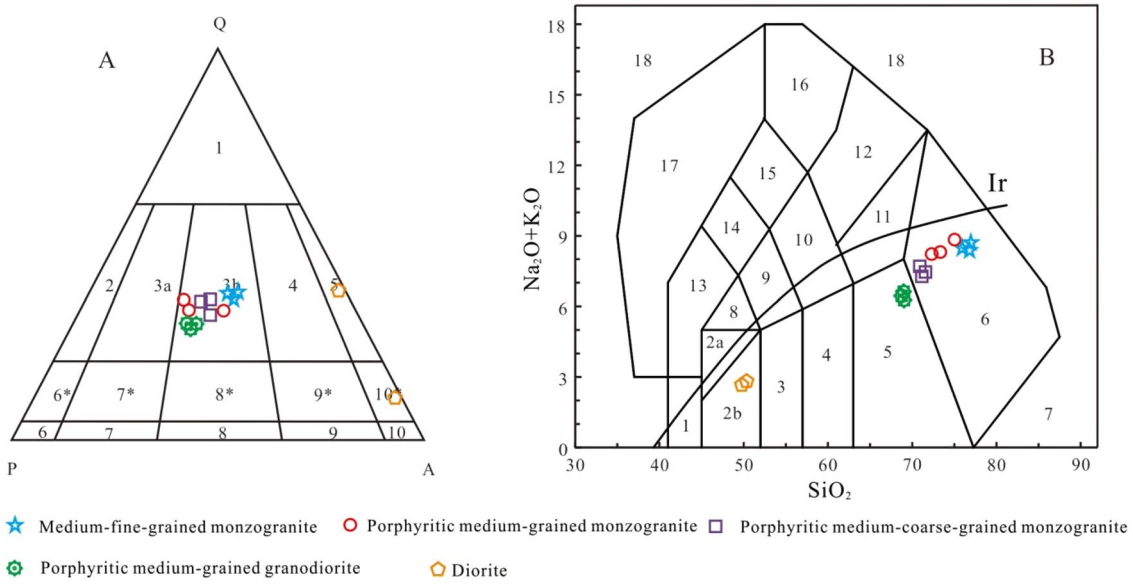

Fig. 6 SiO_2-AR diagram of magmatic rock mass (**A**) and rock series diagram (**B**) [21, 22]

is high and the degree of rock acidity is also high. The magma is high in acidity, with a DI of 84.97–90.53, a high FL of 83.386–87.421 and a high MF of 79.683–84.971, indicating significant separation and crystallization. The Larsen index LI = 23.084–26.758 shows increased values of SiO_2 and K_2O and decreased values of FeO, MgO and CaO. Table 2 clearly shows the CIPW standard minerals, with the rock clearly lacking the standard mineral diopside, but containing the standard mineral corundum. The standard mineral combination of Q, Or, Ab, An, C, Hy clearly shows that the rock belongs to the supersaturated type SiO_2 with supersaturated aluminum.

The porphyritic medium-coarse-grained monzogranite is an acidic rock with a SiO_2 content in the range of 67.90% to 76.60%. The Al_2O_3 content ranges from 12.13% to 14.30%, while the TiO_2 content ranges from 0.14% to 0.45%. The K_2O content is between 3.28% and 5.03%, the Na_2O content between 3.00% and 3.74%. The rock is characterized by a high content of Si, Al and K and a low content of Na, Ca, Mg and Fe. The rock has a calcium-alkaline composition with a Ritman index of $\delta = 1.698–2.268$ and $\delta < 4$. The alkalinity index is AR = 2.476–4.207 and the consolidation index is SI = 1.738–9.343.

Table 2 CIPW standard mineral content of magmatic rocks in the working area

Sample	PM006-4-YH1*	PM006-5-YH1*	PM006-5-YH2*	PM006-6-YH1*	PM006-6-YH2*	PM006-7-YH2*	PM005-12-YH3	PM005-12-YH4	D1683-YH1	PM005-3-YH2	PM005-3-YH3	PM005-3-YH4	D1685-YH1	D1685-YH2*
Name	MFGM	MFGM	MFGM	PMFGM	PMFGM	PMFGM	PMCGM	PMCGM	PMCGM	PMGG	PMGG	PMGG	GD	GD
Or	28.79	27.32	28.72	25.03	28.7	24.65	25.42	26.1	23.98	24.46	23.87	26.07	4.6	4.68
ab	26.72	28.92	28.61	31.66	29.8	31.11	27	26.88	30.44	27.14	27.51	27.01	19.96	20.39
an	3.14	3.43	3.13	7.47	5.75	6.12	8.79	7.97	8.05	13.03	13.3	11.03	31.1	31.19
di										0	0	0	10.62	12.64
c	0.72	0.49	0.54	1.06	0.31	1.68	1.12	1.13	0.54	0.64	0.72	0.77	0	0
hy	2.51	3	2.14	5.37	2.87	5.05	4.36	4.03	1.33	5.65	6	6.53	12.27	24.39
q	37.59	36.51	36.64	28.28	32.03	30.19	31.52	31.94	31	26.6	26.29	26.28	7.52	1.28
ap	0.04	0.04	0.04	0.15	0.09	0.18	0.22	0.24	0.14	0.33	0.33	0.33	0.66	0.66
il	0.15	0.21	0.13	0.62	0.29	0.62	0.81	0.79	0.53	1.14	1.18	1.14	0	4.03
mt	0.34	0.07	0.04	0.35	0.16	0.43	0.76	0.92	3.85	1.02	0.81	0.84	2.12	0.75

MFGM-Medium-fine-grained monzogranite; PMFGM-Porphyritic medium-fine-grained monzogranite; PMCGM-Porphyry medium-coarse-grained monzogranite; PMGG-Porphyritic medium-grained granodiorite; GD-Granodiorite

The rock has a high degree of magma differentiation and high acidity, with a differentiation index of DI = 77.64–91.28 and a rock index of FL = 75. The high value of 615–94.582 indicates a significant degree of magma separation and crystallization. The high acidity of the rock is reflected in the Mafic index MF, which ranges from 63.790 to 90.173, and the Larsen index LI, which ranges from 20.352 to 27.163. This indicates a high content of SiO_2 and K_2O and a low content of FeO, MgO and CaO. Table 2 clearly shows the CIPW standard minerals, with the rock notably lacking the standard mineral diopside but containing the standard mineral corundum. The standard mineral combination of Q, Or, Ab, An, C, Hy clearly shows that the rock belongs to the supersaturated type SiO_2 with supersaturated aluminum.

Porphyritic medium-grain granodiorite is an acidic rock with a SiO_2 content of 68.10% to 68.70%. The rock has a high content of Si, Al and K and is poor in Na, Ca, Mg and Fe. The Al_2O_3 content is between 14.60% and 15.16%, while the TiO_2 content is between 0.59% and 0.64%. The K_2O content is between 3.98% and 4.33%, and the Na_2O content is between 3.14% and 3.21%. It is important to note that K_2O exceeds Na_2O content. The rock is calcium-alkaline with a Ritman index of $\delta = 2.01–2.23$ and $\delta < 4$. Its alkalinity index AR is high with a small interval of 2.33 to 2.57. The consolidation index SI suggests a slightly lower magma differentiation degree of 10.80–11.89. In addition, the acidity of the rock is not high, with a differentiation index DI of 77.67–79. Magma acidity is high and is indicated by a value of 36. The Felsic index is between 71.82 and 75.99, while the Mafic index is low, between 67.44 and 69.95. This suggests a low degree of magma separation and crystallization. The Larsen index ranges from 19.96 to 20.59, indicating low contents of FeO, MgO and CaO and not high contents of SiO_2 and K_2O. Table 2 clearly shows the CIPW standard minerals and shows the absence of diopside and presence of corundum. The standard mineral composition of the rock, which includes Q, Or, Ab, An, C and Hy, clearly classifies it as supersaturated aluminum belonging to the SiO_2 supersaturated type.

This mafic rock consists of diorite with a SiO_2 content between 50.42% and 50.90%. The Al_2O_3 content is between 15.99% and 16.05%; The TiO_2 content is between 2.07% and 2.09%; The K_2O content is between 0.77% and 0.78%, while the Na_2O content is between 2.34% and 2.38%. The analyzed rock sample is low in Si and K, but high in Ti, Al and Na, while being poor in Ca, Mg and Fe. The Litman index ranges from $\delta = 1.304$ to 1.928, indicating that it is a calcium-alkaline rock with an alkalinity index of AR = 1.281 to 4.174 and a consolidation index of SI = 1.471 to 32. The rock has a wide range of variations, a moderately low degree of magma differentiation and a relatively low acidity. The differentiation index ranges from DI = 26.35 to 32.08, the felsic index ranges from FL = 25.081 to 92.415 and the mafic index ranges from MF = 61.612 to 94.595, all of which show a significant degree of magma separation and crystallization. Although the Larsen index is low, ranging from LI = -8.56 to 26.127, the overall properties of the rock indicate a high level of competence and expertise in the field, with higher levels of sodium and aluminum. Calcium, magnesium, sodium and iron are all present in small amounts. Table 2 shows the CIPW standard minerals with the exception of diopside and the inclusion of corundum. The standard mineral composition consists of Q, Or, Ab, An, C and Hy.

The rock type changed gradually from porphyry granodiorite to porphyry monzogranite and finally to monzogranite. SiO_2 content, total alkalinity ($Na_2O + K_2O$), K_2O/Na_2O ratio and alkalinity ratio (AR) all showed a gradual increase. The consolidation index SI decreased while the differentiation index DI increased, indicating an increasing degree of magma differentiation (Table 3).

The Ir-Irvine dividing line is alkaline above and sub-basic below.

Q-P-A block description: (1) Quartz-rich granite; (2) Alkali feldspar granite; (3a) Granite (syenite); (3b) Granite (monzonite); (4) Granodiorite; (6) Alkaline syenite; (6*) Quartz alkali syenite; (7) syenite; (7*) Quartz syenite; (8) monzonite; (8*) Quartz monzonite; (9) monzonite; (9*) Quartz monzonite; (10) diorite; (10*) Quartz diorite;

TAS block description: (1) olivine gabbro; (2) alkaline gabbro; (3) gabbro diorite; (4) diorite; (5) granodiorite; (6) granite; (7) Silica rock; (8) monzonite gabbro; (9) monzonite granite; (10) monzonite; (11) quartz monzonite; (12) syenite; (13) parafeldspar gabbro; (14) parafeldspar two Long diorite; (15) Vice-feldspar monzonite syenite; (16) Vice-long syenite; (17) Vice-long plutonic rock; (18) Coarse leucite.

The distribution of trace elements in diorite, porphyry-granodiorite, porphyry-monzogranite and monzogranite is continuous and generally to the right, as shown by their trace element properties. The analysis clearly shows that the ferrophilic elements Co, Ni and Cr are present in higher concentrations compared to similar granites worldwide, strongly indicating poor metallogenic conditions. Conversely, the incompatible elements K, Rb and Th are significantly enriched. Ba is relatively depleted, while Ta, Nb and Ce show slight enrichment or no abnormality. Sm, Hf and Zr are depleted, and Y and Yb are severely depleted. Crystallization differentiation occurred during magma evolution, as evidenced by the presence of large ionic lithophilic elements such as Nb, Y, U, Th, and K. The distribution pattern of trace element content, as shown in Fig. 23, is closely similar to that of Co-collision granite, confirming the overall properties of Co-collision granite.

The distribution pattern of rare earth elements (Fig. 7) shows consistent right-sloping curves with negative Eu anomalies ($\delta Eu = 0.08–0.92$) in all samples. The distribution pattern of rare earth elements (Fig. 7) shows consistent right-sloping

Table 3 Characteristic value table of magmatic rock mass in the working area

Sample	PM006-4-YH1*	PM006-5-YH1*	PM006-5-YH2*	PM006-6-YH1*	PM006-6-YH2*	PM006-7-YH2*	PM005-12-YH3	PM005-12-YH4	D1683-YH1	PM005-3-YH2	PM005-3-YH3	PM005-3-YH4	D1685-YH1	D1685-YH2*
Name	MFGM	MFGM	MFGM	PMFGM	PMFGM	PMFGM	PMCGM	PMCGM	PMCGM	PMGG	PMGG	PMGG	GD	GD
σ	1.89	1.90	1.98	2.19	2.19	2.08	1.91	1.94	2.05	2.04	2.02	2.17	4.6	4.68
AR	4.23	4.18	4.34	2.95	3.66	2.97	2.73	2.85	2.95	2.38	2.34	2.57	19.96	20.39
SI	1.14	1.55	0.75	5.66	2.58	5.88	6.52	6.17	4.29	10.81	11.01	11.90	31.1	31.19
FL	92.44	91.84	92.64	83.39	87.42	85.53	79.85	81.39	81.87	72.37	71.83	75.99	10.62	12.64
DL	93.10	92.75	93.97	84.97	90.53	85.95	83.94	84.92	85.42	78.20	77.67	79.36	0	0
MF	93.49	91.18	94.17	80.68	84.97	79.68	78.30	79.18	88.77	69.95	69.53	67.44	12.27	24.39
LI	27.93	27.64	28.49	23.08	26.76	23.54	23.12	23.54	21.69	20.13	19.97	20.59	7.52	1.28
A/CNK	1.06	1.04	1.04	1.07	1.02	1.12	1.07	1.07	1.03	1.02	1.03	1.03	0.66	0.66
A/NK	1.18	1.17	1.16	1.36	1.22	1.37	1.44	1.41	1.34	1.56	1.58	1.48	0	4.03

MFGM-Medium-fine-grained monzogranite; PMFGM-Porphyritic medium-fine-grained monzogranite; PMCGM-Porphyry medium-coarse-grained monzogranite; PMGG-Porphyritic medium-grained granodiorite; GD-Granodiorite

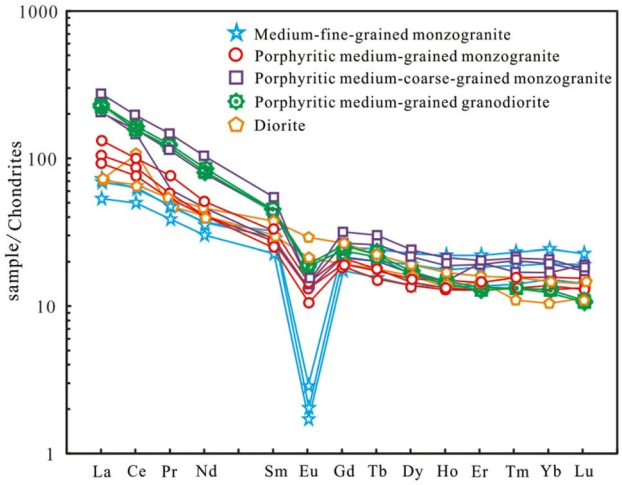

Fig. 7 Normalized rare earth element curve of magmatic rock mass [23]

curves with negative Eu anomalies (δEu = 0.08–0.92) in all samples. The distribution pattern of rare earth elements (Fig. 7) shows consistent right-sloping curves with negative Eu anomalies (δEu = 0.08–0.92) in all samples. The range of variation is significant and changes in lithology lead to an increase in Eu loss. Diagenesis predominantly occurs in a highly oxidized environment. The lithology changes from medium-grained diorite to porphyritic medium-fine-grained granodiorite, then to medium-fine-grained monzogranite, and finally to porphyritic medium-coarse-grained monzogranite. As the lithology changes, the Eu-negative anomaly of the early mafic diorite progressively strengthens, transitioning from weak loss to loss and finally to strong loss. During the crystallization of hornblende and apatite minerals, the text convincingly describes the evolution of loss in Eu. The loss starts weakly in the early stages, progresses in the medium term and culminates in a severe loss in the late stages. This creates a residual melt with a strongly negative Eu anomaly (Table 4). The distribution curves for rare earths show light enrichment types of rare earths that slope to the right (Figs. 8, 9, 10, 11).

5.2 Zircon U–Pb dating

The medium-fine-grained monzogranite yielded a total of 20 age data. The $^{206}Pb/^{238}U$ age change values were projected on or near the U–Pb harmonic curve, and the weighted average age of $^{206}Pb/^{238}U$ was determined to be 219.8 ± 3.0 Ma (MSWD = 2.6; Fig. 12). This age represents the crystallization age of the medium- and fine-grained monzogranite. Sample Pm006-1-Tw1 yielded a weighted average age of 216.6 ± 4.3 Ma (MSWD = 5.8; Fig. 12) based on 20 age change values of $^{206}Pb/^{238}U$ projected on or near the U–Pb harmonic curve. This age represents the crystallization age of the porphyritic medium-coarse-grained monzogranite. Sample Pm006-7-Tw1 yielded a total of 20 age data, with the $^{206}Pb/^{238}U$ age change values projecting on or near the U–Pb harmonic curve. The crystallization age of the porphyritic medium-grained monzogranite was determined to be 215.7 ± 3.3 Ma (MSWD = 2.7; see Fig. 12) based on a weighted average of the $^{206}Pb/^{238}U$ age. This result confidently establishes the age of the sample. Sample Pm005-1-Tw1 yielded a total of 20 age data, with the age change values of $^{206}Pb/^{238}U$ projected on or near the U–Pb harmonic curve. The crystallization age of the porphyritic medium-grained granodiorite was determined to be 221.0 ± 2.7 Ma (MSWD = 2.5; refer to Fig. 12) through calculation of the weighted average age of $^{206}Pb/^{238}U$.

The medium-fine-grained monzogranite provided a total of 20 ages. The age change values of $^{206}Pb/^{238}U$ were projected on or near the U–Pb harmonic curve, and a weighted average age of $^{206}Pb/^{238}U$ was determined to be 219.8 ± 3.0 Ma (MSWD = 2.6; Fig. 12). determined. This age represents the crystallization age of the medium- and fine-grained monzogranite. Sample Pm006-1-Tw1 gave a weighted average age of 216.6 ± 4.3 Ma (MSWD = 5.8; Fig. 12), based on 20 age change values of ^{206} Pb/ ^{238}U projects on or near the U–Pb harmonic curve. This age represents the crystallization age of the porphyritic medium coarse monzogranite. Sample Pm006-7-Tw1 provided a total of 20 ages, with the age change values $^{206}Pb/^{238}U$ projecting on or near the U–Pb harmonic curve. The crystallization age of the porphyritic medium-grain monzogranite was determined to be 215.7 ± 3.3 Ma (MSWD = 2.7; see Fig. 12) based on a weighted average of the $^{206}Pb/^{238}U$ ages. This result certainly represents the age of the sample. Sample Pm005-1-Tw1 provided a total of 20 age dates, with the age change values of $^{206}Pb/^{238}U$ projected on or near the U–Pb harmonic curve. The crystallization age of the porphyritic medium-grained granodiorite was determined to be 221.0 ± 2.7 Ma (MSWD = 2.5; see Fig. 12) by calculating the weighted average age of $^{206}Pb/^{238}U$.

Table 4 Characteristic values of rare earth elements in the magmatic rock mass in the working area

Sample	PM006-4-YH1*	PM006-5-YH1*	PM006-5-YH2*	PM006-6-YH1*	PM006-6-YH2*	PM006-7-YH2*	PM005-12-YH3	PM005-12-YH4	D1683-YH1	PM005-3-YH2	PM005-3-YH3	PM005-3-YH4	D1685-YH1	D1685-YH2*
Name	MFGM	MFGM	MFGM	PMFGM	PMFGM	PMFGM	PMCGM	PMCGM	PMCGM	PMGG	PMGG	PMGG	GD	GD
∑REE	99.49	103	77.82	118.83	111.5	142.5	273.21	215.1	183.52	219.22	216.66	227.6	123.76	107.65
∑Ce	81.29	81.06	63.8	105.58	96.42	128.1	250.44	194.82	166.17	203.8	200.39	211.3	109.64	89.77
∑Y	18.2	21.94	14.02	13.25	15.05	14.4	22.77	20.28	17.35	15.42	16.27	16.32	14.12	17.88
∑Ce/∑Y	4.47	3.69	4.55	7.97	6.41	8.9	11	9.61	9.58	13.22	12.32	12.95	7.76	5.02
La/Yb	4.97	4.13	4.84	11.23	8.35	13.51	17.88	14.5	16.56	25.25	23.57	25.01	9.11	6.56
Sm/Nd	0.26	0.29	0.25	0.2	0.22	0.21	0.17	0.19	0.21	0.17	0.18	0.17	0.24	0.27
Gd/Yb	1.35	1.24	1.38	1.63	1.49	1.85	1.89	1.64	1.54	2.36	2.4	2.48	2.21	2.16
(La/Yb) n	3.35	2.78	3.27	7.57	5.63	9.11	12.06	9.77	11.17	17.03	15.89	16.86	6.14	4.42
(La/Sm) n	2.28	2.2	2.29	4.06	3.3	3.98	4.79	4.55	6.95	5.16	4.86	5.06	2.23	1.82
δEu	0.08	0.1	0.09	0.62	0.46	0.55	0.34	0.39	0.52	0.55	0.55	0.54	0.86	0.92
δCe	1.07	1.02	1.06	1.04	1.02	0.94	0.92	0.97	1.07	0.91	0.91	0.91	1.77	1.04

MFGM-Medium-fine-grained monzogranite; PMFGM-Porphyritic medium-fine-grained monzogranite; PMCGM-Porphyry medium-coarse-grained monzogranite; PMGG-Porphyritic medium-grained granodiorite; GD-Granodiorite

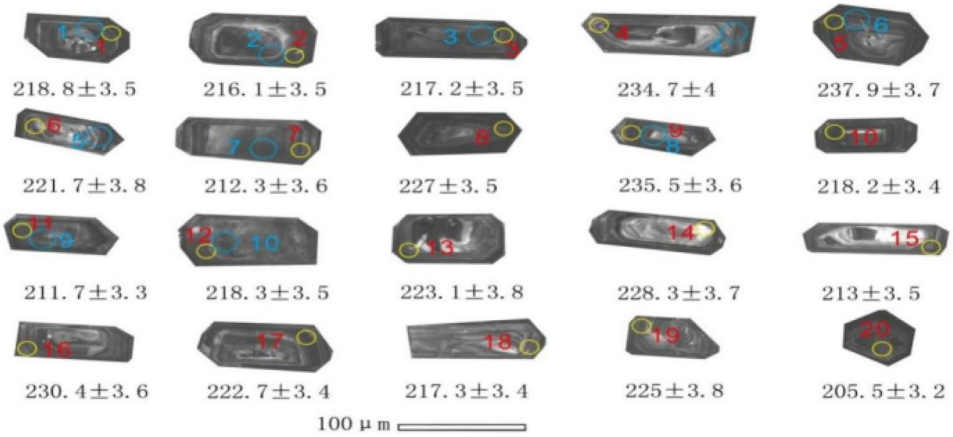

Fig. 8 CL image of fine-grained monzogranite in magmatic rock mass

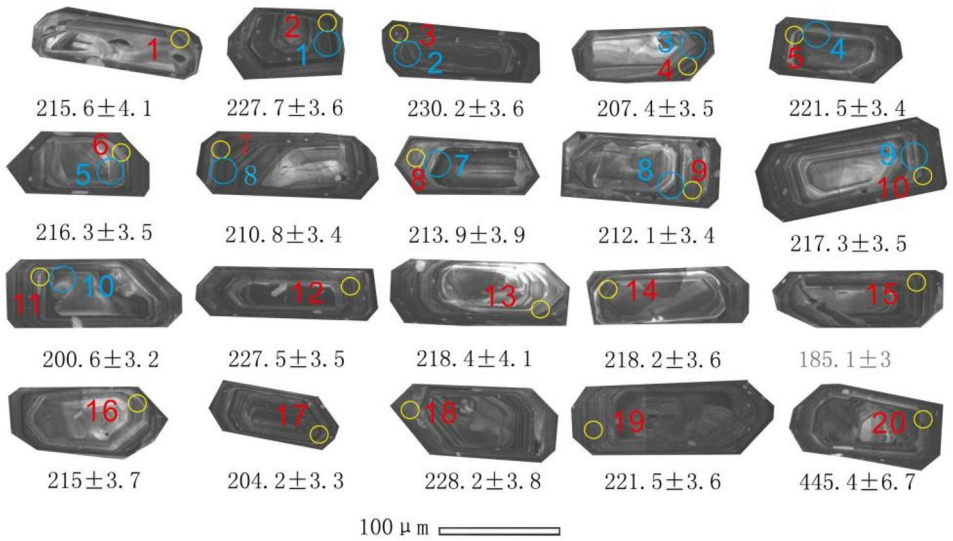

Fig. 9 CL image of zircon of porphyritic medium-grained monzogranite

The medium-fine-grained diorite provided a total of 20 ages projected on or near the U–Pb harmonic curve. Based on the $^{206}Pb/^{238}U$ age change values, a weighted average age of 213.4 ± 1.6 Ma (MSWD = 2.5; Fig. 12) was determined, which represents the crystallization age of the diorite with certainty (Table 5).

This study determined LA-ICP-MS U–Pb age with a high degree of certainty. The ages obtained are as follows: 216.6 ± 4.3 Ma, 215.7 ± 3.3 Ma, 219.8 ± 3.0 Ma, 221.0 ± 2.7 Ma, and 213.4 ± 1.6 Ma. The intrusion time of granodiorite and monzogranite is close to the zircon age of 207 ± 1.6 Ma-230 ± 1.3 obtained from the granite bodies adjacent to Wuhe Mari in the northern Bayankala volcanic belt [24–26]. The order of formation for the syllabic → acidic magma should be porphyritic granodiorite → monzogranite → porphyritic monzogranite. It is very likely that the medium-fine-grained diorite was formed by a separate ejecta. The ages of the various granite rock types in the area agree within the margin of error. Furthermore, the geological observation that there is no clear contact boundary between monzogranite and granodiorite in the igneous rock body further supports this finding. Monzogranite and granodiorite have a similar major element composition (Table 1) and have almost identical distribution patterns of rare earths and trace elements (Fig. 8). Therefore, despite minor differences in their lithofacies, it can be safely assumed that both rocks belong to the same igneous rock mass. The porphyritic medium-fine-grained monzogranite, the porphyritic medium-fine-grained monzogranite, the medium-fine-grained monzogranite, and porphyritic medium-fine-grained granodiorite in the working area are the result of one magmatic activity, while the medium-fine-grained diorite rock is the result of another magmatic activity (Figs. 13, 14, 15, 16, 17).

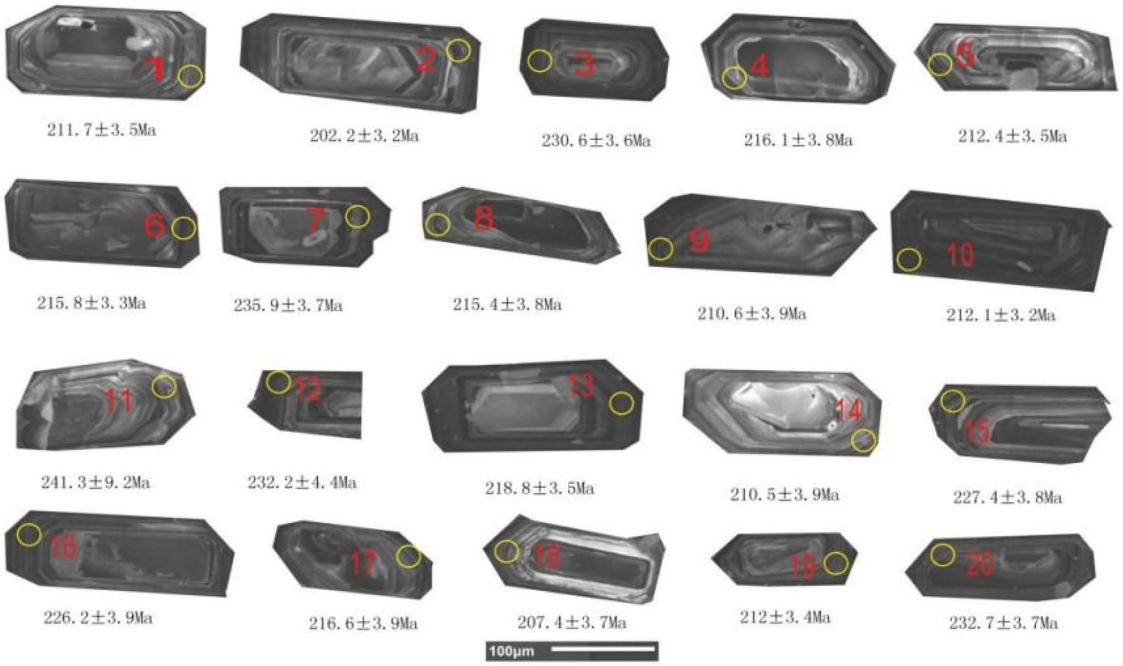

Fig. 10 CL image of zircon of magmatic rock mass like porphyritic medium-grained monzogranite

Fig. 11 Porphyritic medium-grained granodiorite zircon CL image of magmatic rock mass

6 Discussion

6.1 Magmatic genesis

Medium-fine grained diorite has unique major elements not found in other rock types. Figure 18 shows a clear correlation between the increase of SiO_2, Al_2O_3, FeO, CaO, MgO, MnO, Na_2O, P_2O_5, TiO_2 and K_2O and the decrease of porphyritic medium-grained granodiorite, porphyritic medium-coarse-grained monzogranite, porphyritic medium-grained

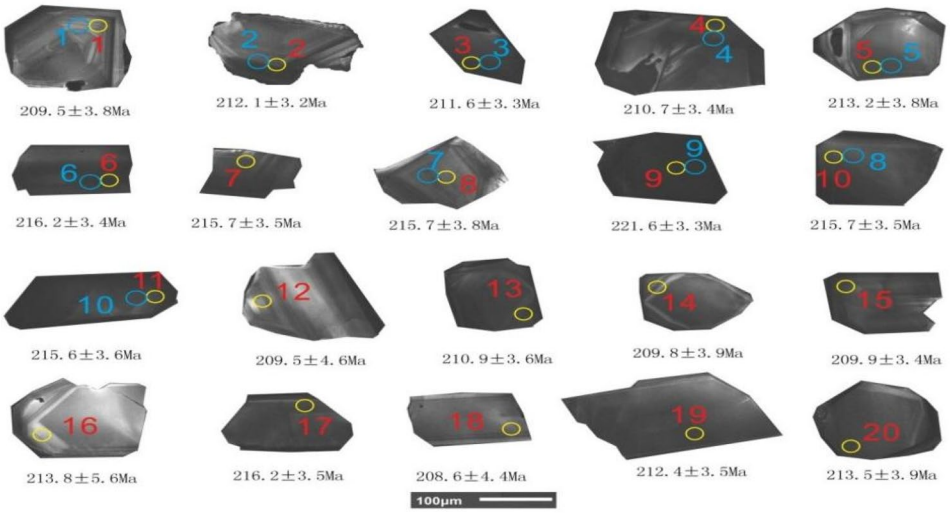

Fig. 12 CL image of fine-grained diorite zircon in magmatic rock mass

granodiorite, fine-grained monzogranite and medium-fine-grained monzogranite. The stage of magma development clearly shows a process of crystallization differentiation attributed to plagioclase, titanium-iron oxides and the separation and crystallization of iron and magnesia minerals and apatite from the melt [26].

All samples were cast on type I granite, as shown in the diagrams of the SiO_2-Ce and SiO_2-Zr lithogenetic series (Fig. 19).

The mineral composition of porphyritic medium-fine-grained granodiorite, porphyritic medium-coarse-grained monzogranite, porphyritic medium-fine-grained monzogranite and medium-fine-grained monzogranite is similar. According to the indication of the content of main elements, the SiO_2 content, the total alkali content ($Na_2O + K_2O$), K_2O/Na_2O and the alkalinity rate (AR) gradually increased from porphyritic medium-fine-grained granodiorite → porphyritic medium-coarse-grained monzogranite → porphyritic medium-fine-grained monzogranite → medium-fine grain niger Monzogranite, the consolidation index SI showed a decreasing trend and the differentiation index DI increased linearly, reflecting the increasing degree of magma differentiation. The distribution characteristics of porphyritic medium-fine-grained granodiorite and porphyritic medium-coarse-grained monzogranite, porphyritic medium-fine-grained monzogranite and medium-fine-grained monzogranite are very consistent in the trace element spider web diagram and the rare earth element distribution diagram.

Porphyritic medium-fine-grained granodiorite, porphyritic medium-coarse-grained monzogranite, porphyritic medium-fine-grained monzogranite and medium-fine-grained monzogranite were formed not directly by partial remelting of the mantle, but by partial melting of the lower crustal rocks, as indicated by the properties of major and trace elements. Significant differences in Th/Yb ratios between different rock types were observed. The mottled medium-fine-grained granodiorite had ratios ranging from 13.75 to 17.28, while the mottled medium-coarse-grained monzogranite had ratios ranging from 8.44 to 8.99. The mottled medium-fine-grained monzogranite had ratios ranging from 8.49 to 10.3, and the ratio for the mottled medium-grained rock was 8.5 to 12. The Th/Yb ratios of the amphibolite, which range from 1.3 to 3.66, certainly indicate that the source area is closer to the mantle, which has been partially remelted. Furthermore, the zircon εHf(t) values of + 13 for the medium-fine-grained diorite provide strong evidence of a sediment contribution to the source area [27–29]. During homologous magmatic differentiation as rare earth elements evolve, residual magma exhibits increasingly obvious europium-negative anomalies as minerals such as plagioclase and potassium feldspar separate and crystallize [30]. The δEu values for the different rock types in this study area were calculated. The mean δEu value for the mottled medium-fine-grained granodiorite is 0.55, while the mean δEu value for the mottled medium-coarse-grained monzogranite is 0.54. The medium-coarse-grained monzogranite has an average δEu value of 0.42 and the medium-fine-grained monzogranite has an average δEu value of 0.09. The homologous magmatic differentiation and evolutionary relationship between porphyritic granodiorite, porphyritic diorite and medium-fine-grained diorite is clearly demonstrated by the variation of δEu. The zircon U–Pb chronology study confirms with certainty that the porphyritic medium-fine-grained granodiorite has an age of 221.0 ± 2.7 Ma, the porphyritic medium-coarse-grained monzogranite has an age of 216.6 ± 4.3 Ma, and the porphyritic medium-fine-grained granodiorite has an age of 216.6 ± 4.3 Ma. The grainy monzogranite has an age of 215.7 ± 3.3 Ma and the medium-fine-grained monzogranite has an age of 219.8 ± 3.0 Ma. Porphyritic granodiorite,

Table 5 Zircon U–Pb isotope test results of magmatic rock bodies

Analysis points	Isotope ratio								Age (Ma)				
	$^{207}Pb/^{206}Pb$	1σ	$^{207}Pb/^{235}U$	1σ	$^{206}Pb/^{238}U$	1σ	rho	$^{207}Pb/^{206}Pb$	1σ	$^{207}Pb/^{235}U$	1σ	$^{206}Pb/^{238}U$	1σ
Pm006-1-Tw1(Porphyritic medium-coarse-grained monzogranite)													
Pm006-1-Tw1-1	0.06784	0.0031	0.31801	0.0154	0.034	0.0007	0.3161	863.5	144	280.4	13	215.6	4
Pm006-1-Tw1-2	0.05287	0.003	0.26214	0.0133	0.03596	0.0005	0.2619	323.4	120	236.4	11	227.7	3
Pm006-1-Tw1-3	0.05818	0.0051	0.29154	0.026	0.03635	0.0007	0.1953	536	213	259.8	21	230.2	4
Pm006-1-Tw1-4	0.05088	0.0026	0.22936	0.0128	0.0327	0.0004	0.2137	235.4	223	209.7	11	207.4	3
Pm006-1-Tw1-5	0.05048	0.002	0.24334	0.0095	0.03497	0.0004	0.2926	217.1	212	221.2	8	221.5	3
Pm006-1-Tw1-6	0.05288	0.0056	0.24881	0.0266	0.03413	0.0008	0.1952	323.5	252	225.6	22	216.3	5
Pm006-1-Tw1-7	0.05986	0.0034	0.27428	0.016	0.03323	0.0005	0.2551	598.5	145	246.1	13	210.8	3
Pm006-1-Tw1-8	0.05236	0.0027	0.24352	0.0127	0.03374	0.0005	0.3071	301	119	221.3	10	213.9	3
Pm006-1-Tw1-9	0.04904	0.0034	0.22609	0.0179	0.03344	0.0006	0.2576	149.6	148	207	14	212.1	4
Pm006-1-Tw1-10	0.05268	0.003	0.24899	0.0131	0.03428	0.0007	0.339	314.9	144	225.8	11	217.3	4
Pm006-1-Tw1-11	0.06386	0.0033	0.27834	0.0151	0.03161	0.0008	0.3361	737	157	249.3	12	200.6	5
Pm006-1-Tw1-12	0.09867	0.0033	0.48867	0.0153	0.03592	0.0006	0.2648	1599.2	158	404	13	227.5	4
Pm006-1-Tw1-13	0.05043	0.0032	0.2396	0.0161	0.03446	0.0006	0.2658	214.8	142	218.1	13	218.4	4
Pm006-1-Tw1-14	0.05113	0.0027	0.24263	0.0133	0.03442	0.0005	0.2635	246.7	126	220.6	11	218.2	3
Pm006-1-Tw1-15	0.06856	0.0026	0.2753	0.0123	0.02913	0.0006	0.3143	885.4	122	246.9	10	185.1	4
Pm006-1-Tw1-16	0.05385	0.0036	0.25171	0.0178	0.03391	0.0007	0.2472	364.4	174	228	15	215	4
Pm006-1-Tw1-17	0.05591	0.002	0.24805	0.0098	0.03218	0.0005	0.336	448.6	60	225	8	204.2	3
Pm006-1-Tw1-18	0.05553	0.0024	0.2759	0.0113	0.03604	0.0005	0.2948	433.1	111	247.4	9	228.2	3
Pm006-1-Tw1-19	0.05093	0.0019	0.2454	0.009	0.03495	0.0004	0.302	237.6	138	222.8	7	221.5	3
Pm006-1-Tw1-20	0.33927	0.0042	3.34562	0.0184	0.07153	0.0007	0.2843	3659.5	181	1491.8	15	445.4	5
Pm006-7-Tw1(Porphyritic medium-grained monzogranite)													
Pm006-7-Tw1-1	0.05367	0.0018	0.24709	0.0084	0.03339	0.0004	0.3352	357.3	80	224.2	7	211.7	2
Pm006-7-Tw1-2	0.07077	0.0036	0.31082	0.0162	0.03186	0.0006	0.2328	950.7	167	274.8	13	202.2	4
Pm006-7-Tw1-3	0.10845	0.0024	0.54456	0.0106	0.03642	0.0005	0.3315	1773.5	105	441.4	9	230.6	3
Pm006-7-Tw1-4	0.04998	0.0033	0.23486	0.0147	0.03409	0.0006	0.3282	193.9	126	214.2	12	216.1	4
Pm006-7-Tw1-5	0.05257	0.0024	0.24274	0.0107	0.03349	0.0005	0.3338	310.4	105	220.7	9	212.4	3
Pm006-7-Tw1-6	0.05362	0.0072	0.25168	0.0316	0.03405	0.001	0.2257	354.9	302	227.9	26	215.8	6
Pm006-7-Tw1-7	0.06788	0.0022	0.34873	0.0114	0.03727	0.0005	0.3144	864.9	89	303.8	9	235.9	3
Pm006-7-Tw1-8	0.06772	0.0031	0.31725	0.0139	0.03398	0.0006	0.2887	859.9	135	279.8	11	215.4	4
Pm006-7-Tw1-9	0.05546	0.0029	0.25391	0.0134	0.03321	0.0005	0.2553	430.6	137	229.7	11	210.6	3
Pm006-7-Tw1-10	0.05276	0.0032	0.24326	0.0154	0.03344	0.0005	0.2451	318.6	128	221.1	12	212.1	3
Pm006-7-Tw1-11	0.05481	0.0022	0.2682	0.0108	0.0355	0.0005	0.2997	404.4	106	241.3	9	224.9	3
Pm006-7-Tw1-12	0.07694	0.0048	0.38909	0.0216	0.03668	0.0013	0.4203	1119.7	211	333.7	18	232.2	8
Pm006-7-Tw1-13	0.06032	0.003	0.28709	0.0155	0.03452	0.0005	0.2761	615.1	109	256.3	12	218.8	3
Pm006-7-Tw1-14	0.0564	0.0047	0.25803	0.0231	0.03319	0.0007	0.216	467.4	200	233.1	19	210.5	4
Pm006-7-Tw1-15	0.0521	0.0048	0.25786	0.0237	0.0359	0.0009	0.294	289.6	191	232.9	19	227.4	6
Pm006-7-Tw1-16	0.05264	0.0031	0.25918	0.0141	0.03571	0.0006	0.3454	313.4	124	234	11	226.2	4
Pm006-7-Tw1-17	0.05145	0.0025	0.24244	0.0118	0.03418	0.0005	0.3315	261.2	105	220.4	10	216.6	3
Pm006-7-Tw1-18	0.05579	0.0044	0.25146	0.0204	0.0327	0.0007	0.2414	443.5	183	227.8	16	207.4	4
Pm006-7-Tw1-19	0.05095	0.0048	0.23485	0.0143	0.03343	0.0007	0.274	238.6	173	214.2	13	212	5
Pm006-7-Tw1-20	0.05199	0.0035	0.26346	0.0164	0.03676	0.0007	0.3364	285	139	237.5	13	232.7	4
Pm006-4-Tw1(Medium-coarse-grained monzogranite)													
Pm006-4-Tw1-1	0.05429	0.0033	0.25832	0.0149	0.03452	0.0006	0.2856	382.9	127	233.3	12	218.8	4
Pm006-4-Tw1-2	0.05255	0.0029	0.24691	0.0131	0.03409	0.0004	0.2304	309.2	95	224.1	11	216.1	3
Pm006-4-Tw1-3	0.05202	0.0028	0.24565	0.0128	0.03426	0.0005	0.2849	286.2	119	223	10	217.2	3
Pm006-4-Tw1-4	0.05204	0.0034	0.26603	0.0149	0.03709	0.0007	0.2992	287.3	164	239.5	12	234.7	4

Table 5 (continued)

Analysis points	Isotope ratio								Age (Ma)				
	$^{207}Pb/^{206}Pb$	1σ	$^{207}Pb/^{235}U$	1σ	$^{206}Pb/^{238}U$	1σ	rho	$^{207}Pb/^{206}Pb$	1σ	$^{207}Pb/^{235}U$	1σ	$^{206}Pb/^{238}U$	1σ
Pm006-4-Tw1-5	0.05306	0.003	0.27486	0.0152	0.03759	0.0007	0.3304	331.2	132	246.6	12	237.9	4
Pm006-4-Tw1-6	0.05097	0.0023	0.24585	0.0109	0.03499	0.0004	0.2635	239.6	103	223.2	9	221.7	3
Pm006-4-Tw1-7	0.05578	0.0032	0.25743	0.0148	0.03349	0.0005	0.2445	443.2	139	232.6	12	212.3	3
Pm006-4-Tw1-8	0.0488	0.003	0.24112	0.015	0.03585	0.0006	0.2632	138.4	137	219.3	12	227	4
Pm006-4-Tw1-9	0.13673	0.003	0.70112	0.0149	0.0372	0.0006	0.2984	2186.1	120	539.5	12	235.5	4
Pm006-4-Tw1-10	0.05696	0.0033	0.27024	0.0154	0.03442	0.0005	0.2381	489.3	87	242.9	13	218.2	3
Pm006-4-Tw1-11	0.0522	0.0033	0.24024	0.0149	0.03339	0.0005	0.2274	294.4	143	218.6	12	211.7	3
Pm006-4-Tw1-12	0.05155	0.0042	0.2447	0.0185	0.03444	0.0007	0.289	265.5	179	222.3	15	218.3	4
Pm006-4-Tw1-13	0.05096	0.0068	0.24732	0.0315	0.03521	0.001	0.2096	239.2	289	224.4	26	223.1	6
Pm006-4-Tw1-14	0.05489	0.0026	0.27269	0.0117	0.03604	0.0004	0.2224	407.7	117	244.8	10	228.3	2
Pm006-4-Tw1-15	0.05317	0.0032	0.24613	0.0161	0.03359	0.0006	0.2658	335.8	142	223.4	13	213	4
Pm006-4-Tw1-16	0.05214	0.0027	0.26146	0.0133	0.03638	0.0005	0.2635	291.7	126	235.8	11	230.4	3
Pm006-4-Tw1-17	0.05255	0.0026	0.25464	0.0123	0.03516	0.0006	0.3143	309.5	122	230.3	10	222.7	4
Pm006-4-Tw1-18	0.04988	0.0036	0.23569	0.0178	0.03428	0.0007	0.2472	189.4	174	214.9	15	217.3	4
Pm006-4-Tw1-19	0.05134	0.0042	0.25131	0.0194	0.03551	0.0006	0.2353	256.3	175	227.6	16	225	4
Pm006-4-Tw1-20	0.07208	0.0038	0.32176	0.0182	0.03239	0.0008	0.2866	987.9	174	283.3	15	205.5	5
Pm005-1-Tw1(Porphyritic medium-grained granodiorite)													
Pm005-1-Tw1-1	0.06376	0.0025	0.31732	0.0113	0.03616	0.0005	0.3286	733.8	88	279.8	9	229	3
Pm005-1-Tw1-2	0.05409	0.0018	0.25325	0.0081	0.03402	0.0003	0.3256	374.6	66	229.2	7	215.6	2
Pm005-1-Tw1-3	0.05317	0.0036	0.25084	0.0149	0.03428	0.0007	0.3517	336	156	227.3	12	217.3	5
Pm005-1-Tw1-4	0.06042	0.0047	0.29071	0.0222	0.03496	0.0007	0.2416	618.7	191	259.1	18	221.5	4
Pm005-1-Tw1-5	0.05562	0.0024	0.2553	0.0113	0.03335	0.0004	0.2757	436.9	109	230.9	9	211.5	3
Pm005-1-Tw1-6	0.05603	0.0034	0.26376	0.0159	0.0342	0.0005	0.2576	453.4	137	237.7	13	216.8	3
Pm005-1-Tw1-7	0.05667	0.0026	0.27128	0.0118	0.03478	0.0006	0.3256	477.9	117	243.7	10	220.4	3
Pm005-1-Tw1-8	0.06879	0.0022	0.33395	0.0104	0.03527	0.0005	0.3247	892.4	93	292.6	8	223.4	3
Pm005-1-Tw1-9	0.10561	0.0019	0.51683	0.0092	0.03555	0.0005	0.4176	1725	71	423	7	225.2	3
Pm005-1-Tw1-10	0.0558	0.002	0.2623	0.0093	0.03415	0.0004	0.2804	444.1	87	236.5	8	216.5	3
Pm005-1-Tw1-11	0.17547	0.0015	0.8548	0.008	0.03538	0.0004	0.3214	2610.5	69	627.3	6	224.2	2
Pm005-1-Tw1-12	0.07431	0.0023	0.36831	0.0103	0.036	0.0005	0.3495	1050	98	318.4	8	228	3
Pm005-1-Tw1-13	0.10304	0.0023	0.48648	0.0123	0.03429	0.0005	0.2825	1679.6	-86	402.5	10	217.3	3
Pm005-1-Tw1-14	0.05453	0.0018	0.26931	0.0087	0.03587	0.0004	0.3184	393	80	242.1	7	227.2	2
Pm005-1-Tw1-15	0.05477	0.0027	0.25495	0.0131	0.03381	0.0005	0.2714	402.8	115	230.6	11	214.3	3
Pm005-1-Tw1-16	0.05335	0.0027	0.25878	0.0124	0.03523	0.0006	0.3576	343.7	103	233.7	10	223.2	4
Pm005-1-Tw1-17	0.06426	0.0048	0.32209	0.02	0.0364	0.0006	0.2345	750	189	283.5	16	230.5	4
Pm005-1-Tw1-18	0.29091	0.0022	1.23074	0.0123	0.03072	0.0004	0.2757	3422.5	87	814.7	8	195.1	3
Pm005-1-Tw1-19	0.05541	0.0019	0.27044	0.0087	0.03545	0.0005	0.2576	428.4	69	243	7	224.5	4
Pm005-1-Tw1-20	0.07647	0.002	0.39993	0.02	0.03798	0.0006	0.3256	1107.5	98	341.6	8	240.3	2
D1685-Tw1(Medium-fine-grained diorite)													
D1685-Tw1-1	0.05031	0.0025	0.22892	0.0113	0.03302	0.0005	0.3286	209.2	88	209.3	9	209.5	3
D1685-Tw1-2	0.05059	0.0018	0.23315	0.0081	0.03345	0.0003	0.3256	222.2	66	212.8	7	212.1	2
D1685-Tw1-3	0.05157	0.0036	0.23711	0.0149	0.03337	0.0007	0.3517	266.6	156	216.1	12	211.6	5
D1685-Tw1-4	0.04882	0.0047	0.22348	0.0222	0.03322	0.0007	0.2416	139	191	204.8	18	210.7	4
D1685-Tw1-5	0.04926	0.0024	0.22827	0.0113	0.03363	0.0004	0.2757	160.2	109	208.8	9	213.2	3
D1685-Tw1-6	0.04976	0.0034	0.23389	0.0159	0.03411	0.0005	0.2576	183.9	137	213.4	13	216.2	3
D1685-Tw1-7	0.05212	0.0026	0.24441	0.0118	0.03403	0.0006	0.3256	290.5	117	222	10	215.7	3
D1685-Tw1-8	0.04994	0.0022	0.2342	0.0104	0.03403	0.0005	0.3247	192.2	93	213.7	8	215.7	3
D1685-Tw1-9	0.049	0.0019	0.23619	0.0092	0.03498	0.0005	0.4176	147.7	71	215.3	7	221.6	3

Table 5 (continued)

Analysis points	Isotope ratio								Age (Ma)				
	$^{207}Pb/^{206}Pb$	1σ	$^{207}Pb/^{235}U$	1σ	$^{206}Pb/^{238}U$	1σ	rho	$^{207}Pb/^{206}Pb$	1σ	$^{207}Pb/^{235}U$	1σ	$^{206}Pb/^{238}U$	1σ
D1685-Tw1-10	0.05008	0.002	0.23479	0.0093	0.03402	0.0004	0.2804	198.7	87	214.1	8	215.7	3
D1685-Tw1-11	0.05259	0.0015	0.24654	0.008	0.03402	0.0004	0.3214	311	69	223.8	6	215.6	2
D1685-Tw1-12	0.05025	0.0023	0.2333	0.0103	0.03369	0.0005	0.3495	206.6	98	212.9	8	213.6	3
D1685-Tw1-13	0.05288	0.0023	0.24239	0.0123	0.03326	0.0005	0.2825	323.8	-86	220.4	10	210.9	3
D1685-Tw1-14	0.05161	0.0018	0.23537	0.0087	0.03309	0.0004	0.3184	268.3	80	214.6	7	209.8	2
D1685-Tw1-15	0.04882	0.0027	0.22271	0.0131	0.0331	0.0005	0.2714	139.2	115	204.2	11	209.9	3
D1685-Tw1-16	0.05276	0.0027	0.24518	0.0124	0.03371	0.0006	0.3576	318.5	103	222.7	10	213.8	4
D1685-Tw1-17	0.05252	0.0034	0.24691	0.0159	0.03411	0.0005	0.2576	308	71	224.1	11	216.2	3
D1685-Tw1-18	0.05393	0.0026	0.24449	0.0118	0.03289	0.0006	0.3256	368	87	222.1	12	208.6	4
D1685-Tw1-19	0.05083	0.0022	0.23477	0.0104	0.03351	0.0005	0.3247	233.3	121	214.1	14	212.4	4
D1685-Tw1-20	0.04949	0.0048	0.22975	0.02	0.03368	0.0006	0.2345	170.9	189	210	16	213.5	4

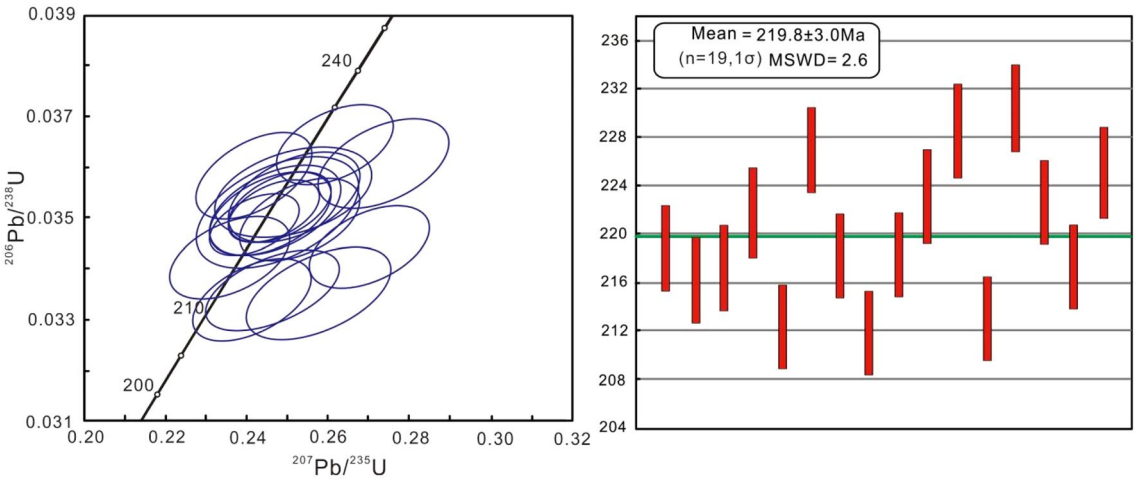

Fig. 13 Fine-grained monzogranite zircon U–Pb age in magmatic rocks

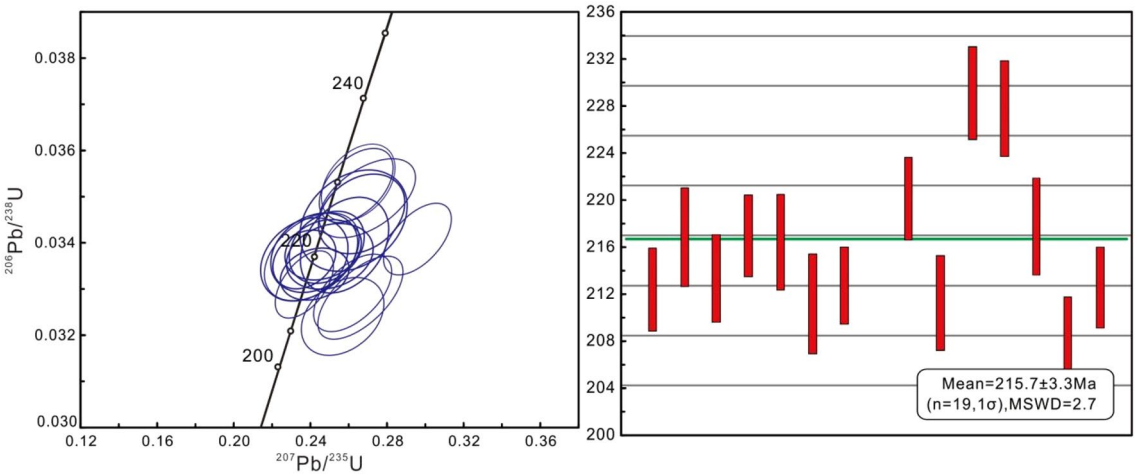

Fig. 14 The magmatic rock mass resembles porphyritic, medium-grained monzogranite and zircon U–Pb age

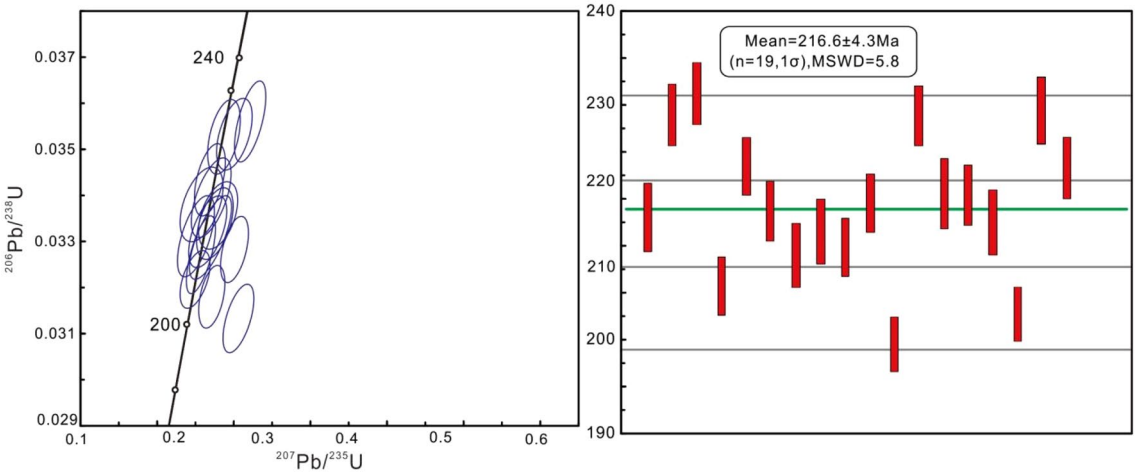

Fig. 15 The magmatic rock mass resembles porphyritic medium-coarse-grained monzogranite with zircon U–Pb age

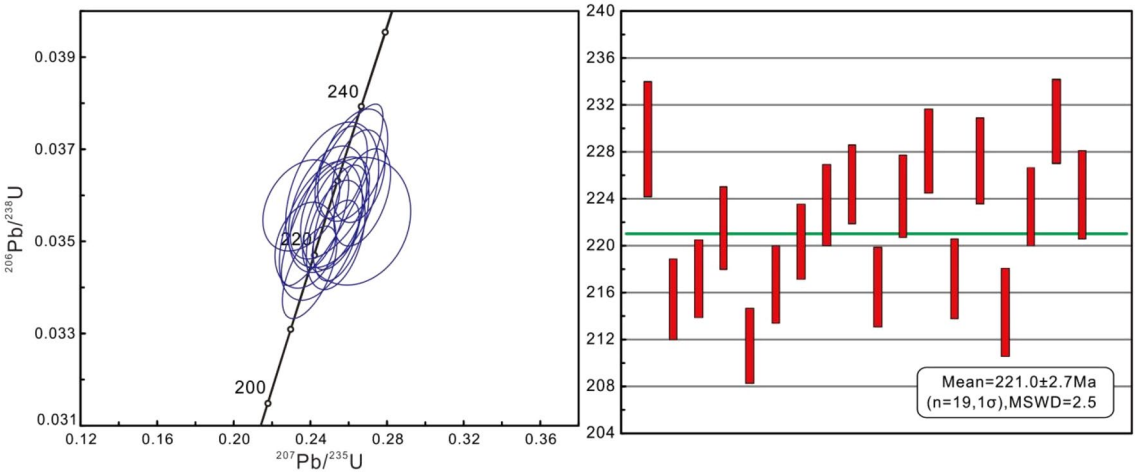

Fig. 16 The magmatic rock mass resembles porphyritic medium-grained granodiorite zircon U–Pb age

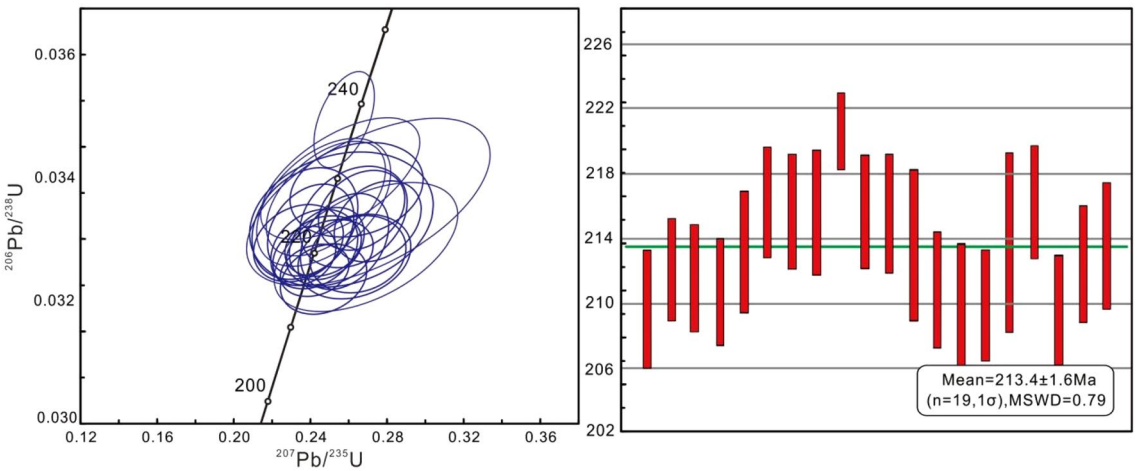

Fig. 17 Zircon U–Pb age of fine-grained diorite in magmatic rock mass

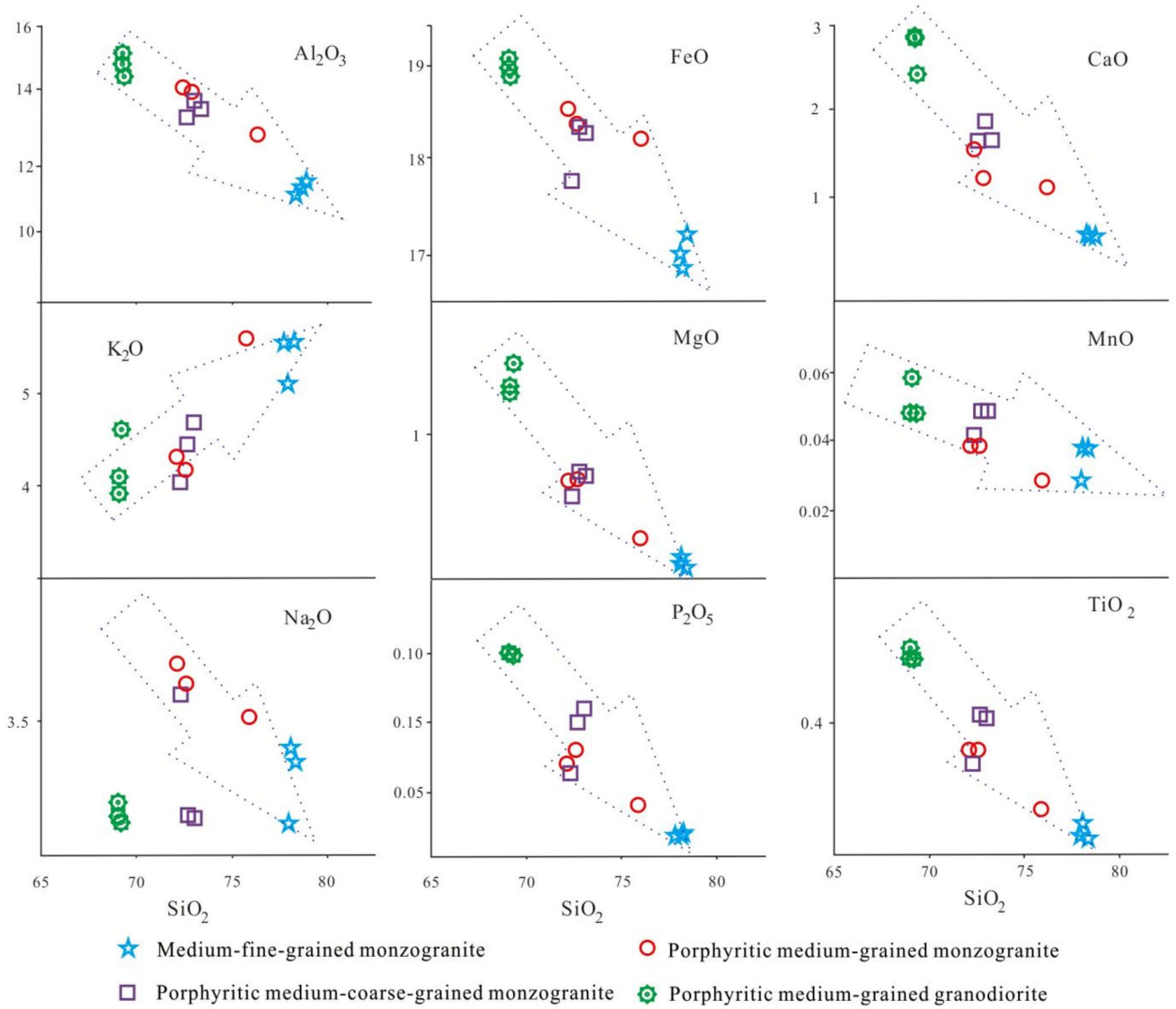

Fig. 18 Harker diagram of magmatic rock mass

porphyritic diorite and monzogranite were formed simultaneously. The order of formation in the magma body is first porphyric granodiorite, followed by monzogranite and then porphyric diorite.

The porphyritic granodiorite, monzogranite and porphyritic diorite are rock assemblages formed by the same magma melting event, as evidenced by their petrographic and mineralogical features, rock geochemical analyses, and zircon U–Pb chronology. It is unlikely that the diorite is a product of the same magma melting event. The sequence of magma development consists of porphyritic granodiorite, monzogranite and porphyritic diorite. These rocks are the result of crystalline differentiation of homologous magmas.

6.2 Analysis of the tectonic setting of magmatic bodies

Studying the geochemical properties of igneous rocks is crucial to understanding the tectonic environment in which they were formed. These properties vary depending on the environment in which they emerged. The composition of igneous rocks is clearly determined by the composition of the source region. The geochemical properties of trace elements in igneous rocks formed under different tectonic environments show significant differences.

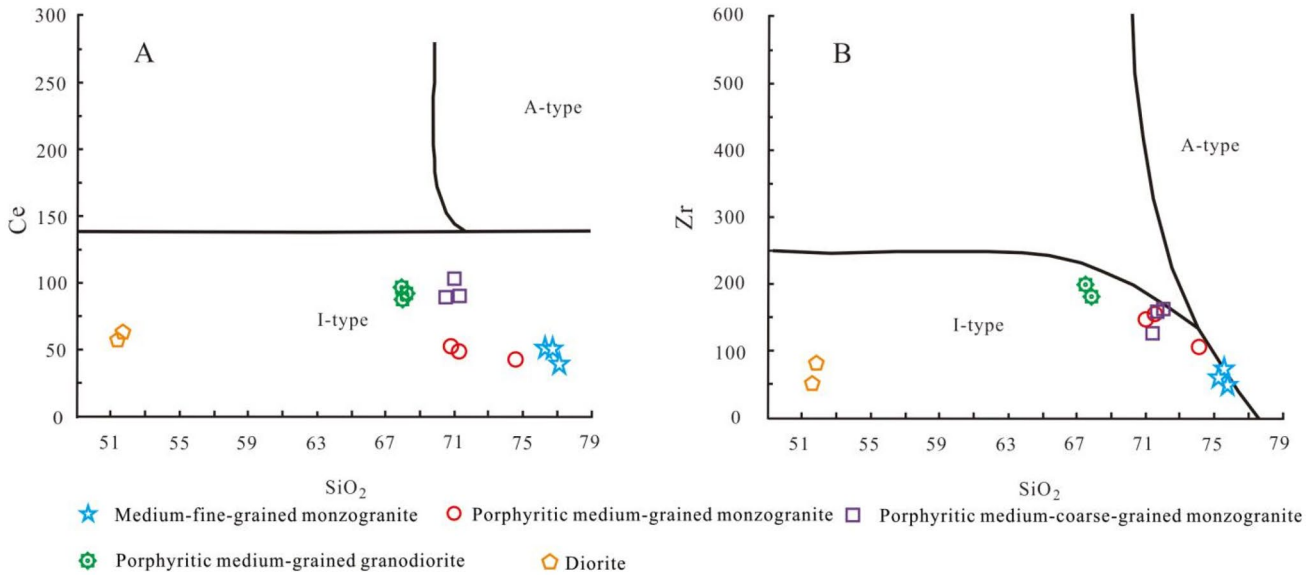

Fig. 19 Diagram of SiO2-Ce (**A**) and SiO2-Zr (**B**) of the lithogenetic series

Figure 20 clearly illustrates the covariance between R1-R2. It is worth noting that monzogranite, porphyritic monzogranite, and porphyritic granodiorite are all located in the same collision region, with preplate collision diorite predominantly falling within the region.

Data analysis included mapping using Hf-Rb/10-Ta × 3 triangles versus Hf-Rb/30-Ta × 3 triangles for casts (Fig. 21). In the Hf-Rb/10-Ta × 3 map (Fig. 21A), it can be seen that the diorite, porphyritic diorite and porphyritic granodiorite casts fall within the granodiorite range in the context of a collisional geotectonic setting, while the amphibolite Casts fall into the granodiorite area fall into the granodiorite area within the slab. In the Hf-Rb/30-Ta × 3 diagram (Fig. 21B), diorite, porphyritic monzogranite and porphyritic granodiorite are confidently located near volcanic arc granite and collisional granite, while amphibolite is confidently found in intraplate granite.

The Pearce et al. developed granite tectonic environment distinction diagram was reliably used to map the samples. In the Ta-Yb diagram, all samples were clearly classified as volcanic arc granite (VAG), with a few falling near the collisional granite (syn-COLG) boundary (see Fig. 22A). The sample is certainly located in the syn-COLG region of the Rb-Yb + Ta map, while the diorite certainly belongs to the volcanic arc granite (VAG) region, as shown in Fig. 22B. The sample is safely located in the volcanic arc granite (VAG) and syn -COLG (SYN-Colg) region on the Nb-Y map (Fig. 22C). Similarly, in the Rb-Yb + Nb diagram, the sample is positioned in the syn-COLG region (Fig. 22D).

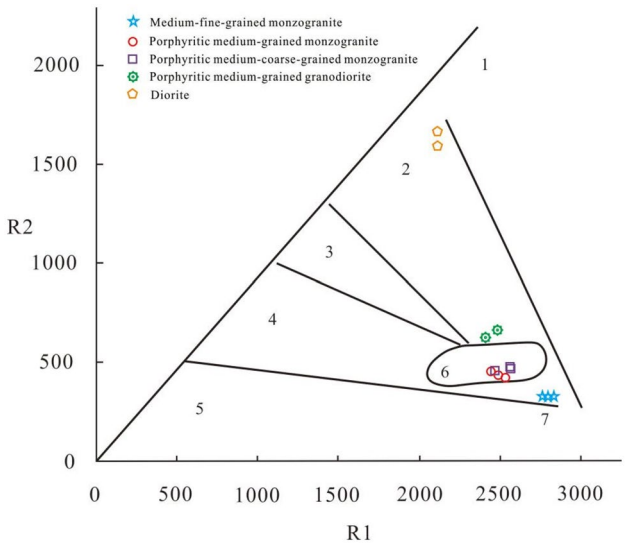

Fig. 20 Diagram of R1-R2 covariation of magmatic rocks [31]. R1 = 4Si-11(Na + K)-2(Fe + Ti), R2 = 6Ca + 2 Mg + Al (thousands of cations). 1. Mantle differentiation product; 2. Before plate collision; 3. Post-collision uplift; 4. Late orogenic; 5. Non-orogenic; 6. Syn-collision; 7. Post-orogenic

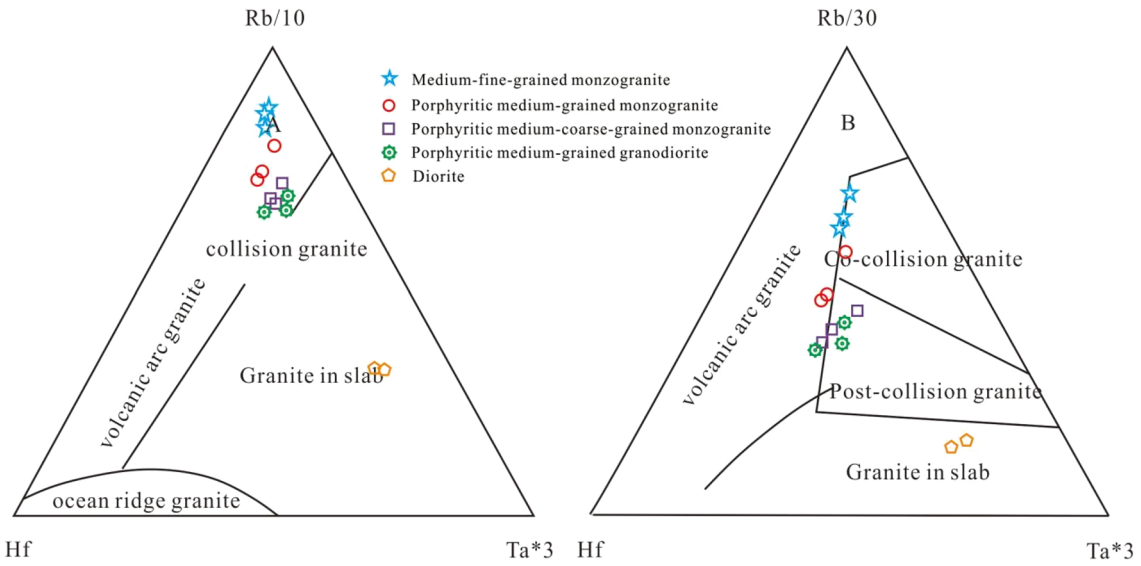

Fig. 21 Discrimination diagram of tectonic environment of magmatic rocks Hf-Rb/10-Ta × 3(A) and Hf-Rb/30-Ta × 3(B)[32]

Figure 20 shows that the example projection points in the R1-R2 plot fall predominantly on collisional and post-orogenic aged granites. Figure 21 shows a discriminant diagram comparing the tectonic environments of Hf-Rb/10-Ta × 3(A). and Hf-Rb/30-Ta × 3(B). The diagram clearly shows that monzogranite, porphyritic monzogranite and porphyritic granodiorite occur near volcanic arc granite and collisional granite, while diorite occurs in the granite region within the plate. This suggests a strong correlation between the composition of these rocks and their tectonic setting. The samples in the granite-tectonic-environmental distinction diagram (Fig. 22) of Pearce are certainly located in the area of the volcanic arc granite (VAG) and syn-COLG [33]. The rare earth element schematic spider web diagram, standardized on oceanic ridge granite, has similarities with volcanic arc granite and co-collision granite. It consistently exhibits the properties of co-collision granite.

Zircon U–Pb chronology confirms that the diagenetic age of the monzogranite, porphyritic monzogranite and porphyritic granodiorite is between 215.7 ± 3.3 Ma and 221.0 ± 2.7 Ma, while the diagenetic age of the diorite 213.4 ± 1.6 Ma. These ages are consistent with the evolution from cocollisional granite to intraplate granite (Fig. 23).

The Late Triassic granite in the study area was formed by post-collision uplift as a result of frictional heat and crustal thickening in the intracontinental extrusive environment during the Late Triassic. This conclusion is based on the given features and analysis of the tectonic background. The production of crustal source magma was caused by the local melting of the crustal rocks. The new magma, created by the deep melting of the crustal rocks, safely intruded into the area along the northwest-southeast trending fault zone (subduction zone), forming the composite rock foundation of the Late Triassic intrusive rocks.

From the above discussions, monzogranite, porphyritic monzogranite and porphyritic granodiorite are formed in the synclinal tectonic environment, while diorite is formed in the intraplate tectonic environment.

6.3 Tectonic evolution

During the Middle Triassic, the Paleo-Tethys Ocean continued to subduct northward, resulting in the folding of the Muzitag, Kunlun and Animaqing areas on the northern side of the Bayankala Basin into mountains. The Bayankala Basin lithosphere was deflected with the closure of the Paleo-Tethys Basin, forming a marginal foreland basin. During the Middle to Late Triassic, mountains emerged, causing seawater to retreat and the marginal foreland basin to disappear. The Bayankala Basin granite has been dated using zircon U–Pb dating, yielding an age range of 207–230 Ma [24, 34]. The authors determined a zircon U–Pb age of 213.8 ± 2.0 Ma in the adjacent study area, while the zircon U–Pb age of the Jiangri Karma granite intrusive rock was 222.5 ± 1.9 Ma amounts.

Northward subduction of the Paleo-Tethys Ocean continued into the Upper Triassic, which is supported by the above findings. Furthermore, the intensification of subduction-reduction of the ocean basin resulted in upwelling of mantle material in the asthenosphere, resulting in thinning and subsidence of the lithosphere [35]. Aldanmaz and

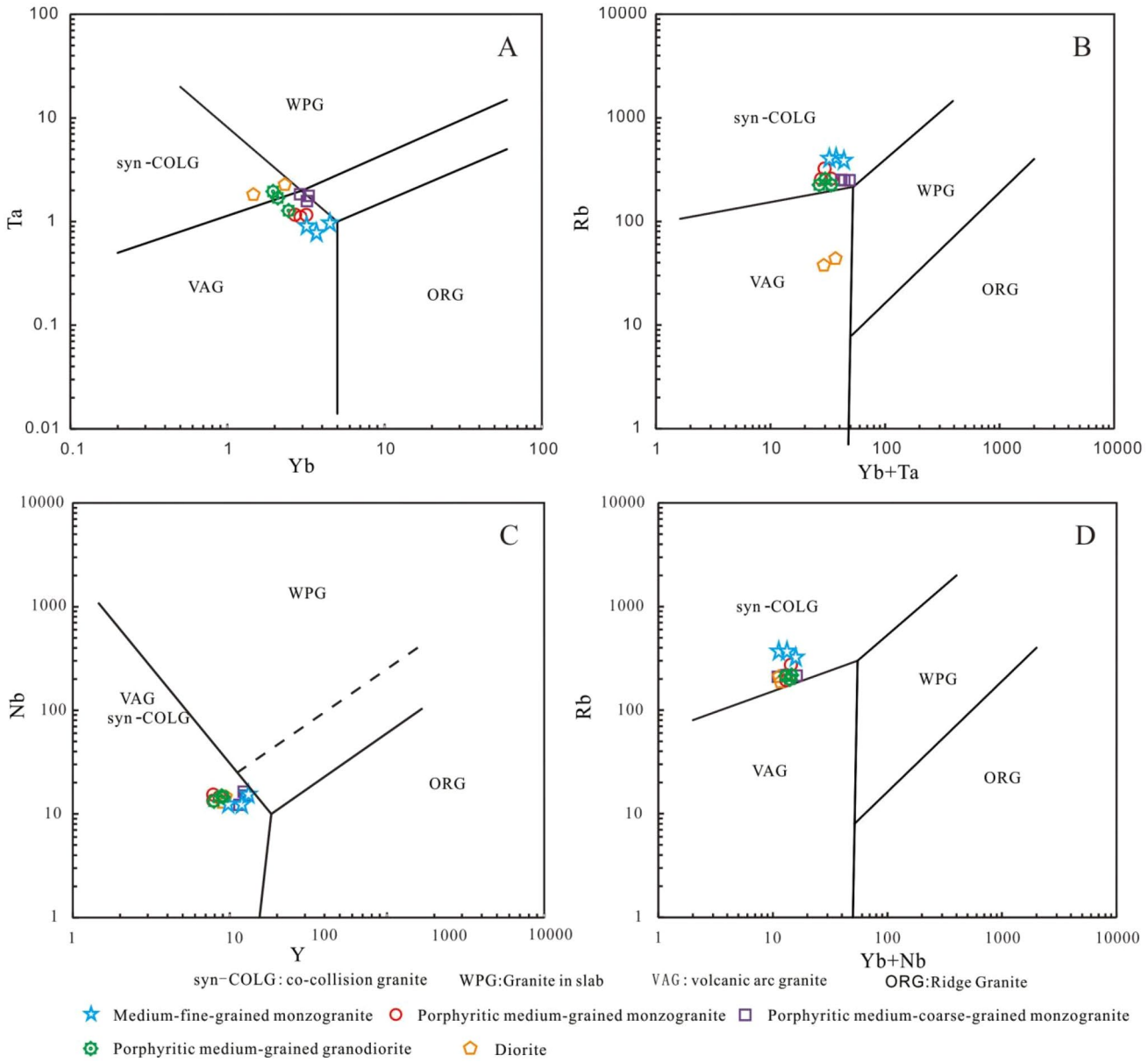

Fig. 22 Diagram for judging the tectonic environment of magmatic plutons [33]

Ilbeyli certainly observed partial melting of the metasomatized mantle wedge material [36, 37], which conclusively led to the formation of basaltic magma (Fig. 24a). The formation of a basaltic magma chamber at the interface between the lower crust and the mantle was a direct result of the increasing amount of basaltic magma, as shown in Fig. 24b. About 221 million years ago, basaltic magma chambers transferred a significant amount of thermal energy to the upper crust, resulting in melting of the upper crust and the formation of granitic magma with high supersaturation of silicon, alkali, and aluminum. This granitic magma is the original magma of the granite complex in Wuhe Mari area. The granitic magma rises to the surface by diapiric action and intrudes into the porphyritic granodiorite in the northeast of the work area (Fig. 24c). At about 216 million years ago the remaining magma crystallized in the deep subsurface and created porphyry. This porphyry was then transported to shallow condensation crystallization, resulting in the formation of porphyry monzogranite. In addition, some of the magma underwent further crystallization and differentiation, eventually forming monzogranite on the surface. Detachment slip of the lithospheric mantle during the formation of the orogenic belt in the Late Triassic led to the development of multi-stage overburden structures between the upper and lower crust of the crust and the mantle, and between the upper crust and the overburden.

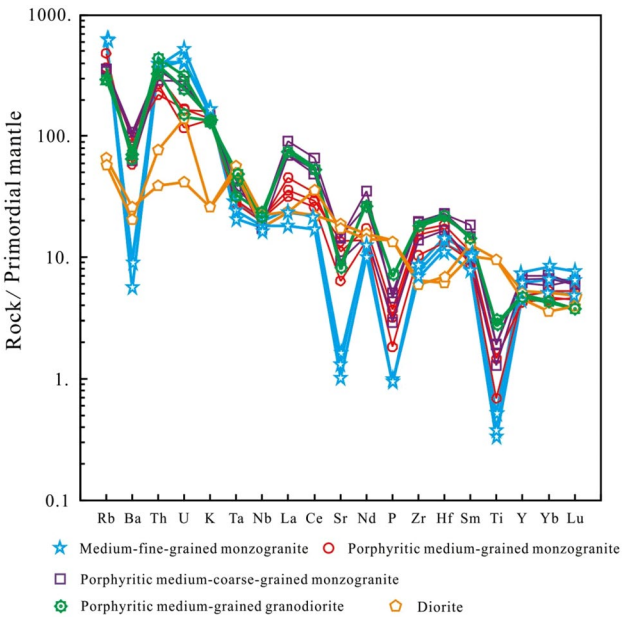

Fig. 23 Normalized curve of trace elements in magmatic rock mass [23]

This process caused the co-collisional granite to transform into intraplate granite. Diorite formed around 213 Ma when deep mafic magma rose to the surface in regions with thinner crust (Fig. 24d).

7 Conclusion

This paper confidently presents a study on the petrological and zircon U–Pb chronology of the Wuhe Mari granite complex. The study draws the following conclusions:

The magmatic rock mass in the study area consists of fine-grained monzogranite, porphyritic granodiorite, and porphyritic monzogranite, all of which belong to the acid rock type and display a moderate to strong negative europium anomaly. The samples exhibit high levels of Si and Al_2O_3, as well as K, and low levels of Na, Ca, Mg, Fe, Rb, and Th. They also show strong enrichment in incompatible elements, mild enrichment or no abnormality of Ta, Nb, Ce, Sm, Hf, and Zr, and significant loss of Y and Yb. The aluminum saturation index of the samples is < 1.1, indicating that they belong to type I granite formed in the same collision environment. The rock is confidently identified as a mafic diorite with medium and fine grains. Its composition is characterized by low levels of Si and K, but high levels of Ti, Al, and Na. Additionally, it exhibits poor levels of Ca, Mg, and Fe, and an aluminum saturation index of less than 1.1. Based on these features, it can be confidently classified as belonging to the intraplate environment of type I granite.

The porphyritic granodiorite, monzogranite, and porphyritic monzogranite are rock assemblages formed by the same magmatic melting event. The petrographic and mineralogical characteristics, petrogeochemical analysis results, and zircon U–Pb chronology all support this conclusion. It is clear that the three rocks are the result of homologous magmatic evolution. The magmatic evolution sequence begins with porphyritic granodiorite, followed by monzogranite, and ends with porphyritic monzogranite. The text is grammatically correct and free from spelling and punctuation errors. Diorite is formed when co-collisional granite evolves into intraplate granite, and metamafic magma in the deep crust rises to the surface. The language used is clear and objective, and the technical terms are used consistently. No changes in content have been made as per the given instructions.

According to the petrogeochemical characteristics and the age comparison of zircon U–Pb, the rock geochemical characteristic curves of porphyritic granodiorite, monzogranite and porphyritic monzogranite in the magmatic rock mass in the Wuhe Mari area are in good agreement with the upper crustal curve, The material in the source area is the result of the melting of upper crustal material, formed through the crystallization and differentiation of homologous magma. Its formation environment is associated with a collisional tectonic environment. Similarly, the diorite formation environment is associated with an intraplate tectonic environment.

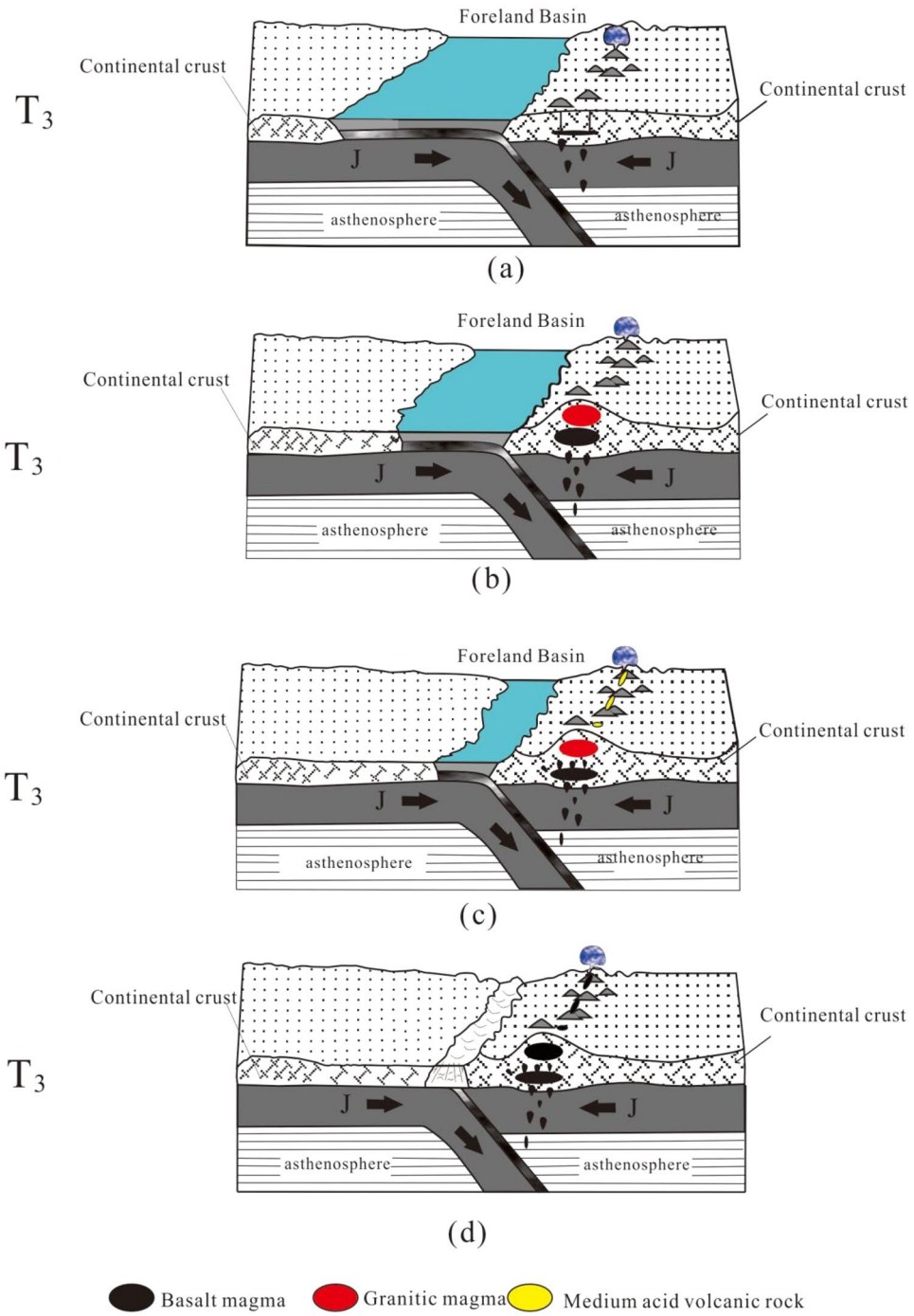

Fig. 24 The genetic model of the magmatic rock mass in the study area [26]

Acknowledgements The work presented in this article is supported by a project by the China Geological Survey (12120114009001), (12120113071300) and (DD20242769). The reviewers and editors would like to express their sincere gratitude for their constructive revisions to the manuscript.

Author contribution Guanghao Tian: Validation, Supervision, Project administration, Formal analysis, Conceptualization. Yanbing Zong: Resources, Investigation. Yanping Xue: Resources, Investigation.

Funding The work presented in this article is supported by a project by the China Geological Survey (12120114009001), (12120113071300) and (DD20242768).

Data availability Data will be made available on request.

Declarations

Competing interests The authors declare no competing interests.

References

1. Honglie S, Du Z. Comprehensive Investigation and Scientific Research on the Qinghai-Tibet Plateau. China Association for Science and Technology.Scientific and Technological Progress and Discipline Development-Proceedings of the Annual Conference on "Science and Technology Facing the New Century". China Qinghai-Tibet Plateau Research Association; China Tibetan Plateau Research Association. 1998.
2. Jishun R, Guigui N, Zhigang L. Soft collision, overlapping orogeny and multi-cyclic seam synthesis. Earth Sci Front. 1999;03:85–93.
3. Yanlin G. Discussion on the restoration and reconstruction of paleooceanic crust on the Tibetan Plateau. Qinghai Geology. 2000;01:1–8.
4. Guowei Z, Yunpeng D, Shaocong L, Anlin G, Qingren M, Shaofeng L, Shunyou C, Anping Y, Zongqing Z, Xianzhi P, Sanzhong L. Qinling-Dabie Orogenic Belt Southern Margin Mianluo Tectonic Belt and Mianluo Suture Zone. Sci China (Ser D: Earth Sci). 2003;12:1121–35.
5. Guowei Z, Shunyou C, Anlin G, Yunpeng D, Shaocong L, Anping Y. Re-understanding of the Mianluo Ancient Suture Zone on the southern margin of the Qinling-Dabie Central Orogenic System-Also on the assemblage of the main body in Chinese mainland. Geol Bull. 2004;Z2:846–53.
6. Guitang P, Dicheng Z, Liquan W, Zhongli L, Quanru G, Xinsheng J. Pangong Lake-Nujiang suture zone as geological and geophysical evidence for the northern boundary of Gondwana continent. Front Geosci. 2004;04:371–82.
7. Hongfu Y, Fengqing Y, Xulong L. Indosinian ecological stratigraphy and gold biometallogenic study in the West Qinling Mountains and Songpan area. Hubei Province, China University of Geosciences. 2004;01:01.
8. Kexin Z, Qixiang L, Yunhai Z, Hongfu Y, Mansheng L, Nengsong C, Guocan W. New paleontological evidence and its tectonic significance determined by the construction age of mixed rocks in the eastern section of East Kunlun. Sci China (Ser D: Earth Sci). 2004;03:210–8.
9. Yifu Z. Characteristics of Hoh Xili-Bayankala and the adjacent Tethys Sea. Qinghai Geol. 1991;01:1–10.
10. Yifu Z. A preliminary study on the evolution of geological structure in Qinghai and adjacent areas. Plateau Earthq. 1994;03:10–6.
11. Yifu Z. Classification and evolution of the Triassic sedimentary basin of Hoh Xili-Bayankala. Qinghai Geol. 1996;01:1–17.
12. Xingzhen L, Xiaosong X, Guitang P. Evolution of Pan-Chinese continental group and East Tethys tectonic domain. Lithofacies Paleogeogr. 1995;04:1–13.
13. Xueting Z. 1:1,000,000 Qinghai Province Geotectonic Map and Description.Qinghai Province, Qinghai Provincial Institute of Geological Survey. 2005;09-05.
14. Chaofeng Z. Triassic sedimentary filling and tectonic evolution in Bayankala Basin. Northwest University. 2019.
15. Zhiqin Xu, Jingsui Y, Wenchang L, Huaqi L, Zhihui C, Zhen Y, Changqian M. Paleo-Tethys system and accretive orogeny in the Qinghai-Tibet Plateau. Acta Petrologica Sinica. 2013;29(06):1847–60.
16. Baochun H, Yonggang Y, Piper JDA, Donghai Z, Zhiyu Y, Shan Y, Tinghong Z. Paleomagnetic constraints on the paleogeography of the East Asian blocks during Late Paleozoic and Early Mesozoic times. Earth-Sci Rev. 2018;1:S0012825218300862.
17. Guitang P, Xingzhen Li, Liquan W. Preliminary division of geotectonic units in the Qinghai-Tibet Plateau and adjacent Areas. Geol Bull. 2002;11:701–7.
18. Kejun H, Yanhe L, Yourong T. LA-MC-ICP-MS zircon micro-zone in-situ U-Pb dating technology. Geol Ore Depos. 2009;28(04):481–92.
19. Streckeisen A. Classification and nomenclature of plutonic rocks: recommendations of the IUGS subcommission on the systematics of igneous rocks. Geol Rundsch. 1974;63:773–86.
20. Irvine TH, Baragar WRA. A guide to the chemical classification of the common volcanic rocks. Can J Earth Sci. 1971;8(5):523–48.
21. Peccerillo A, Taylor SR. Geochemistry of eocene calc-alkaline volcanic rocks from the Kastamonu area, Northern Turkey. Contrib Miner Petrol. 1976;58(1):63–81.
22. Altherr R, Holl A, Hegner E, et al. High-potassium, calc-alkaline I-type plutonism in the European Varis-cides: northern Vosges (France) and northern Schwarz-wald (Germany). Lithos. 2000;50(1):51–73.
23. Sun SS, McDonough WE. Chemical and isotopic systematics of oceanic basalts: Implications for mantle composition and processes. In: Saunders AD, Norry MJ (eds). Magmatism in the Ocean Basins: Geological Society of London, Special Publication. 1989; 42(1):313–345.
24. Xi W, Yonglin C, Guodian B, Tielin Z, Yanhui W. Age and significance of zircon U-Pb of acid intrusive in Bayan Kala Mountain Group. Miner Explor. 2003;14(06):839–48. https://doi.org/10.2008/j.kckc.202306002.
25. Guanghao T, Xinzhuo H, Ming W, Xiaoyang W. Geochemistry and chronology of granodiorite in the Qubianlang slope area of northern Bayankala. Geol Resource. 2023;32(04):383–93. https://doi.org/10.13686/j.cnki.dzyzy.2023.04.002.
26. Guanghao T, Jianping Q, Meng Q. The genesis of granite mass in the volcanic area of Litang, Chuanxi province: constraints from rock geochemistry and U-Pb zircon dating. Environ Earth Sci. 2023;82(6):1.
27. Sylvester PJ. Post-collisional strongly peraluminous granites. Lithos. 1998;45(1–4):29–44.

28. Jianjun H, Yundong Li, Chuanzhong S, Jun He, Han Xu, Changwei Qi, Mingfu Z, Xiaoliang He. Zircon U–Pb dating and geochemistry of granite in the Reshui area of Dulan County, eastern section of east Kunlun orogen and its tectonic implications. Acta Geol Sin. 2020;94(3):768–81.
29. Elburg MA, van Bergen M, Hoogewerff J, Foden J, Vroon P, Zulkarnain I, Nasution A. Geochemical trends across an arc-continent collision zone: magma sources and slab-wedge transfer processes below the Pantar Strait volcanoes, Indonesia. Geochim Cosmochim Acta. 2002;15:2771–89.
30. Xuezhen S. Genesis and geological significance of dark particulate inclusions in Gangtang fault rock mass in Qiangtang, Tibet. China University of Geosciences(Beijing). 2013.
31. Batchelor RA, Bowden P. Petrogenetic interpretation of granitoid rock series using multicationic parameters. Chem Geol. 1985;48(1–4):43–55.
32. Harris NBW, Pearce JA, Tindle AG. Geochemical characteristics of collision-zone magmatism. Geol Soc Lond Spec Publ. 1986;19(1):67–81.
33. Pearce JA, Harris NBW, Tindle AG. Trace element discrimination diagrams for the tetonic interpretation of granitic rocks. J Petrol. 1984;25:956–83.
34. Mengmeng X, Gao Wanli Hu, Daogong ZY, Jiucheng Xu, Liyun J, Chaoqun W. Zircon U–Pb age and geological significance of volcanic rocks of Bayankala Mountain Group in the northern part of the Qinghai-Tibet Plateau. Mod Geol. 2019;33(05):957–69. https://doi.org/10.19657/j.geoscience.1000-8527.2019.05.03.
35. Pearce JA, Bender JF, De Long SE, Kidd WSF, Low PJ, Güner Y, Saroglu F, Yilmaz Y, Moorbath S, Mitchell JG. Genesis of collision volcanism in Eastern Anatolia, Turkey. J Volcanol Geoth Res. 1990;44:189–229.
36. Aldanmaz E, Pearce JA, Thirlwall MF, Mitchell JG. Petrogenetic evolution late Cenozoic, post-collision volcanism in western Anatolia, Turkey. J Volcanol Geoth Res. 2000;102:67–95.
37. Ilbeyli N, Pearce JA, Thirlwall MF, Mitchell JG. Petrogenesis of collisionrelated plutonic in Central Anatolia. Turkey Lithos. 2004;72:163–82.